Reconstructing the shape and material parameters of dissipative obstacles using an impedance model

Travis Askham* Carlos Borges†

July 18, 2024

Abstract

In inverse scattering problems, a model that allows for the simultaneous recovery of both the domain shape and an impedance boundary condition covers a wide range of problems with impenetrable domains, including recovering the shape of sound-hard and sound-soft obstacles and obstacles with thin coatings. This work develops an optimization framework for recovering the shape and material parameters of a penetrable, dissipative obstacle in the multifrequency setting, using a constrained class of curvature-dependent impedance function models proposed by Antoine, Barucq, and Vernhet in "High-frequency asymptotic analysis of a dissipative transmission problem resulting in generalized impedance boundary conditions." *Asymptotic Analysis*, 26(3-4):257–283, (2001). We find that in certain regimes this constrained model improves the robustness of the recovery problem, compared to more general models, and provides meaningfully better obstacle recovery than simpler models. We explore the effectiveness of the model for varying levels of dissipation, for noise-corrupted data, and for limited aperture data in the numerical examples.

1 Introduction

Inverse scattering problems arise in many applications, including sensing [45, 70], ocean acoustics [30, 34], medical imaging [52, 55, 59, 66], nondestructive testing [35, 38, 53], and radar and sonar [33]. The general setting of those problems is characterized by probing a domain with one or multiple incident waves and obtaining measurements of the scattered waves. From this scattered wave data, one seeks to reconstruct some property of the domain, e.g. density, sound-speed, impedance, shape, etc.

*Department of Mathematical Sciences, New Jersey Institute of Technology, Newark, NJ, USA. *Email: askham@njit.edu*

†Department of Mathematics, University of Central Florida, Orlando, FL, USA. *Email: carlos.borges@ucf.edu*

In this work, we consider the problem of recovering the shape and physical parameters of homogeneous, penetrable obstacles from measurements of the scattered field in the far field region through the use of an impedance model approximation of the standard transmission model. We consider dissipative obstacles in which acoustic waves in the medium are damped and acoustic energy dissipates into thermal energy [18]. In the frequency domain, the dissipation corresponds to a complex wavenumber for the medium of the form $k_1 = \omega\sqrt{(1+\imath\delta/\omega)}/c_1$, where ω is the pulsating frequency of the incident wave, c_1 is the sound speed of the medium, and $\delta > 0$ is the dissipation constant for the medium.

Let Ω_1 denote the interior of a dissipative obstacle with boundary Γ and let $\mathbf{n}$ denote the outward normal on Γ. Given the incident field, u^{inc}, the scattered field, u^{scat}, is modeled by the Helmholtz equation with a transmission boundary condition. In the notation of [4], we have

$$\begin{aligned}
-(\Delta + k_2^2)u^{\text{scat}} &= 0 && \text{in } \Omega_2\ , \\
-(\Delta + k_1^2)u^{\text{scat}} &= k_2^2(1-N^2)u^{\text{inc}} && \text{in } \Omega_1\ , \\
\left[u^{\text{scat}}\right] &= 0 && \text{on } \Gamma\ , \\
\left[\chi\partial_n u^{\text{scat}}\right] &= -\left[\chi\partial_n u^{\text{inc}}\right] && \text{on } \Gamma\ , \\
\sqrt{|\mathbf{x}|}\left(u^{\text{scat}} - \imath k_2\frac{\mathbf{x}}{|\mathbf{x}|}\cdot\nabla u^{\text{scat}}\right) &\to 0 && \text{as } |\mathbf{x}|\to\infty\ ,
\end{aligned} \tag{1}$$

where $\Omega_2 = \mathbb{R}^2\backslash\overline{\Omega_1}$; $k_2 = \omega/c_2$ is the wavenumber of the incoming incident wave; c_2 is the sound speed of the background medium Ω_2 and $c_r = c_1/c_2$ is the relative sound speed; $N = \sqrt{(1+\imath\delta/\omega)}/c_r$ is the relative refractive index; ρ_1 and ρ_2 are the densities for Ω_1 and Ω_2, respectively, and $\rho_r = \rho_1/\rho_2$; $\alpha = 1/(\rho_r(1+\imath\delta/\omega))$ is the complex contrast coefficient; and the function χ is equal to 1 in Ω_2 and α in Ω_1. The notation $[\phi]$ denotes the difference between the exterior and interior traces, or the "jump", of the function ϕ across Γ.

The transmission problem (1) can be solved using standard boundary integral equation methods (BIEMs); see Appendix A.1 for details. Like the case of impenetrable obstacles, say with sound-soft or sound-hard boundary conditions, the solution of a penetrable transmission problem can then be discretized using unknowns on the boundary of the domain alone. However, the transmission problem generally requires the solution of a system of twice the size.

Remark 1. *The difference in computational effort between the penetrable and impenetrable cases is even more significant in the inverse obstacle setting. The Fréchet derivative of the PDE solution with respect to the material parameters typically involves the solution of an inhomogeneous PDE for the penetrable case; see, e.g., [29, §A.2].*

In an attempt to decrease the computational and memory costs in the solution of the problem, several authors proposed to approximate the forward transmission problem by a forward scattering problem for an impenetrable obstacle with a generalized impedance boundary condition (GIBC), see [3, 5, 41,

46, 58, 60–64, 71]. Such approximations hold in various settings, including scattering from penetrable, dissipative objects and objects with thin, penetrable coatings.

In [5], the authors observe that for large dissipation constant, i.e. $\delta \gg 1$, the wave does not penetrate the medium significantly and they show that the forward transmission problem can be approximated asymptotically by a related problem with a GIBC. In particular, if u^{scat} is the solution of (1), then there exists a local operator $\mathcal{Y}$ such that $u^{\text{scat}} \approx \phi$, where

$$\begin{aligned} -(\Delta + k_2^2)\phi &= 0 && \text{in } \Omega_2 \ , \\ (\partial_n - \mathcal{Y})\,\phi &= -\,(\partial_n - \mathcal{Y})\,u^{\text{inc}} && \text{on } \Gamma \ , \\ \sqrt{|\mathbf{x}|}\left(\phi - ik_2\frac{\mathbf{x}}{|\mathbf{x}|}\cdot\nabla\phi\right) &\to 0 && \text{as } |\mathbf{x}| \to \infty \ . \end{aligned} \tag{2}$$

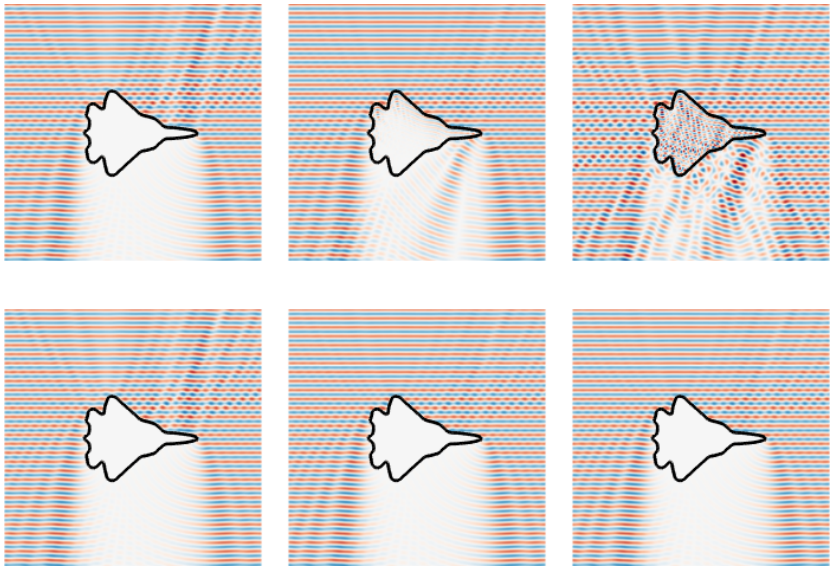

Figure 1: Comparison of the total field of the solution of the transmission ($u = u^{\text{scat}} + u^{\text{inc}}$) and impedance ($u = \phi + u^{\text{inc}}$) scattering problems for $\omega = 30$. The top row shows the transmission solution and the bottom row shows the solution of the first order impedance model. The dissipation decreases from left to right. The first column sets $\delta = \delta_0 = \sqrt{3}\omega$. The second and third columns have $\delta = \delta_0/16$ and $\delta = \delta_0/256$, respectively.

It is possible to obtain different order approximations for the operator $\mathcal{Y}$. For example, the first order operator derived in [5] is a multiplication operator of the form

$$[\mathcal{Y}_1\phi](\mathbf{x}) = -\alpha(\imath k_2 N + H(\mathbf{x}))\phi(\mathbf{x}) \ , \tag{3}$$

where $H(\mathbf{x})$ is the signed curvature at $\mathbf{x} \in \Gamma$. Higher order GIBCs involve differentiation operators on the curve [5, 41].

Figure 1 compares the solution of (1) to the solution of (2) with $\mathcal{Y} = \mathcal{Y}_1$ for the same incident field and varying dissipation. With dissipation in the regime recommended by [4] ($\delta = \delta_0 = \sqrt{3}\omega$), the impedance model agrees well with the transmission model. Slightly below this regime ($\delta = \delta_0/16$), the models still agree well in much of the exterior; however, the solution of the transmission problem exhibits a wave transmitting through the narrowest part of the plane, which is not captured by the impedance model. For even lower values of dissipation ($\delta = \delta_0/256$), the solution of the transmission problem penetrates the obstacle and the solutions of the two models are notably different.

We will explore the suitability of a simple multiplicative GIBC of the form $[\mathcal{Y}\phi](\mathbf{x}) = -\imath k_2 \lambda(\mathbf{x};\omega)\phi(\mathbf{x})$ as an approximate forward model in the inverse obstacle scattering setting with multiple frequency data. More concretely, we consider scattering data for a fixed set of material parameters: c_1, c_2, ρ_1, ρ_2, and δ. We assume that scattering measurements are available for N_k pulsation frequencies, $\omega_1 < \omega_2 < \cdots < \omega_{N_k}$. The incident fields are plane waves of the form $u^{\text{inc}}(\mathbf{x}) = \exp(\imath k_2 \mathbf{d} \cdot \mathbf{x})$ and data are available for $N_d(\omega)$ angles of incidence at each ω, with directions determined by the unit vectors $\mathbf{d}_1, \ldots, \mathbf{d}_{N_d}$. The scattered fields are measured for each incident wave at $N_r(\omega)$ receptor locations, $\mathbf{r}_1, \ldots, \mathbf{r}_{N_r}$, far from the obstacle.

Let the forward transmission operator be defined by $\mathcal{F}^{\text{trans}}_{\omega,\mathbf{d}}(\Gamma) = \mathbf{u}^{\text{out}} \in \mathbb{C}^{N_r}$, where $\mathbf{u}^{\text{out}}_j = u^{\text{scat}}(\mathbf{r}_j)$ and u^{scat} is the solution of the transmission scattering problem, (1). Similarly, let the forward impedance operator be defined by $\mathcal{F}^{\text{imp}}_{\omega,\mathbf{d}}(\Gamma, \lambda) = \mathbf{u}^{\text{out}} \in \mathbb{C}^{N_r}$, where $\mathbf{u}^{\text{out}}_j = \phi(\mathbf{r}_j)$ and ϕ is the solution of the impedance scattering problem, (2), with $\mathcal{Y} = -\imath k_2 \lambda$.

Let $\Gamma_\star$ be the true boundary curve of interest and let $\mathbf{u}^{\text{meas}}_{\omega,\mathbf{d}} = \mathcal{F}^{\text{trans}}_{\omega,\mathbf{d}}(\Gamma_\star)$. At a given frequency ω_j, a natural definition for the "best-fit" boundary curve and GIBC is then given as the solution of the following constrained optimization problem:

$$\left[\hat{\Gamma}_j, \hat{\lambda}_j\right] = \underset{\Gamma \in S_\Gamma(\omega_j), \lambda \in S_\lambda(\omega_j)}{\arg\min} \sum_{i=1}^{N_d} |\mathbf{u}^{\text{meas}}_{\omega_j,\mathbf{d}_i} - \mathcal{F}^{\text{imp}}_{\omega_j,\mathbf{d}_i}(\Gamma, \lambda)|^2 \,, \tag{4}$$

where the sets $S_\Gamma(\omega)$ and $S_\lambda(\omega)$ are chosen to be appropriate spaces for the curve and GIBC at a given pulsation, and can be designed to regularize the problem.

The problems defined by (4) are generally nonlinear, non-convex, and ill-posed. Following the continuation-in-frequency approach [12, 15, 20, 22, 32, 67], we solve these problems in sequence beginning at the lowest frequency, where the problem is approximately convex, and use the solution $\hat{\Gamma}_{j-1}, \hat{\lambda}_{j-1}$ as an initial guess for $\hat{\Gamma}_j, \hat{\lambda}_j$. This helps to mitigate the non-convexity. We apply standard iterative methods to handle the non-linearity and we select the sets S_Γ and S_λ to mitigate the ill-posedness. We then take the recovered boundary and impedance function to be the solution of (4) for the highest frequency data available.

We provide details of the constraint sets, impedance models, and gradient formulas in Section 2. We describe the constraint set for the geometry, S_Γ, in

detail in Section 2.1. We present three options for describing the impedance function λ (and appropriate constraint sets S_λ) in Section 2.2: a general model based on a Fourier series in arc-length and two more-constrained models which depend on the curvature function on Γ. While Fréchet derivative formulae are known for the impedance boundary value problem, the curvature-dependent models require some new expressions which we derive in Section 2.3.

We describe some details of the iterative optimization framework we use at each frequency in Section 3. The curvature-dependent impedance models are more amenable to the imposition of physical constraints, which can be handled effectively by projected gradient methods as described in Section 3.4.

Numerical results are presented in Section 4. These indicate that the solution scheme has greater success with the curvature-dependent models in certain regimes. Domain recovery is effective well below the level of dissipation needed for qualitative agreement between the impedance and transmission forward problems and the curvature-dependent models provide a meaningful advantage over some simpler alternatives. We find that the dissipation, δ, and the product $c_r\rho_r$ can be recovered reliably, with sufficient dissipation, but recovering the values c_r and ρ_r individually appears to be difficult.

We discuss some implications of these results and possible future directions in Section 5.

1.1 Relation to the literature

The inverse problem of recovering the shape and boundary conditions using single frequency data and a model with the classical impedance boundary conditions was studied by several authors [1, 43, 49, 50, 54, 57, 65, 68]. The single frequency inverse scattering problem using the generalized impedance boundary condition model was considered in [10, 23–25, 28, 40, 44, 47, 48, 73]. The use of multifrequency data by applying continuation in frequency to recover the sound speed of a volume was studied in [12, 15, 22, 32], to recover the shape of an impenetrable domain was studied in [20, 67], and to recover the classical impedance boundary condition simultaneously with the shape of obstacle was studied in [21].

The present work introduces a new framework to simultaneously recover the shape of an obstacle and an appropriate impedance function for multifrequency transmission data from a dissipative obstacle. We build on techniques previously presented in [21], in particular the use of continuation-in-frequency for the inverse problem and high-order-accurate methods for solving the associated PDEs via integral equation representations. We provide some necessary formulae and identify effective optimization schemes for treating curvature-dependent impedance models, like the first order model, (3), of [5], in the inverse scattering setting.

2 Details of the model and gradient formulas

This section describes some details of the problem discretization and the constraint sets which regularize the problem at each frequency. The discretization of the obstacle boundary curve and appropriate constraints are described in Section 2.1. A couple of competing models for the impedance function and appropriate constraints for these are described in Section 2.2. Two of the proposed models have an impedance function that depends on the curvature of the obstacle; to apply an iterative method for the solution of (4) with these models, we then require some new derivative formulas that we derive in Section 2.3.

2.1 Representation of the obstacle and its constraints

Let $\mathbb{T}$ be the unit torus, $[0, 1]$. We represent a boundary curve, Γ, by a parameterization $\boldsymbol{\gamma} : \mathbb{T} \to \mathbb{R}^2$, where $\boldsymbol{\gamma}(t) = (x(t), y(t))$, with $x, y : \mathbb{T} \to \mathbb{R}$, being trigonometric polynomials of the form

$$\begin{aligned} x(t) &= a_{1,0} + \sum_{m=1}^{N(\omega)} \left(a_{1,m}\cos(2\pi m t) + b_{1,m}\sin(2\pi m t)\right) \ , \\ y(t) &= a_{2,0} + \sum_{m=1}^{N(\omega)} \left(a_{2,m}\cos(2\pi m t) + b_{2,m}\sin(2\pi m t)\right) \ , \end{aligned} \tag{5}$$

where $a_{j,0}$ and $a_{j,m}$, and $b_{j,m}$ for $j = 1, 2$ and $m = 1, \ldots, N(\omega)$ are real constants and $N(\omega)$ is an integer proportional to ω.

To ensure that the inverse problem at frequency ω is well-posed, we require that the parameterization of the curve, $\boldsymbol{\gamma}$, have bandlimited curvature in a suitable sense. The signed curvature H for a curve-parameterization $\boldsymbol{\gamma}$ is defined as

$$H[\boldsymbol{\gamma}] = \frac{x'y'' - x''y'}{(x'^2 + y'^2)^{3/2}} \ . \tag{6}$$

Here and below, the notation $H[\boldsymbol{\gamma}]$ refers to the parameterization of the curvature on $\mathbb{T}$, while H refers to the curvature as a function on Γ. We define arc-length scaled Fourier coefficients of H by

$$\begin{aligned} a_{H,0} &= \frac{1}{L}\int_\Gamma H \, ds \\ a_{H,m} &= \frac{2}{L}\int_\Gamma H\cos(2\pi m s/L)\, ds \\ b_{H,m} &= \frac{2}{L}\int_\Gamma H\sin(2\pi m s/L)\, ds \end{aligned}$$

where s is an arclength function on Γ and L is the length of the curve. We then define $\mathcal{E}(\Gamma)$, and $\mathcal{E}^{M(\omega)}(\Gamma)$ to be the elastic energy of the curve Γ and the elastic

energy contained in the first $M(\omega)$ modes of the curvature, respectively, i.e.

$$\mathcal{E}(\Gamma) = \int_\Gamma H^2 \, ds \,,$$
$$\mathcal{E}^{M(\omega)}(\Gamma) = \int_0^1 \left(a_{H,0} + \sum_{m=1}^{M(\omega)} \left(a_{H,m} \cos(2\pi m s/L) + b_{H,m} \sin(2\pi m s/L) \right) \right)^2 ds \,. \tag{7}$$

Selecting a value of $M(\omega)$ proportional to ω and a value of C_H near 1, we can impose a bandlimited curvature requirement as the constraint such that $\sqrt{\mathcal{E}^{M(\omega)}} \geq C_H \sqrt{\mathcal{E}(\Gamma)}$.

In addition to this constraint on the curvature, we impose that the curve is simple, i.e. non-self-intersecting. The constraint set for the boundary curves is then

$$\mathcal{S}_\Gamma(\omega) = \{\Gamma \,|\, \Gamma \text{ is simple and } \sqrt{\mathcal{E}^{M(\omega)}(\Gamma)} \geq C_H \sqrt{\mathcal{E}(\Gamma)}\} \,.$$

Beyond the constraint set, the problem can also be regularized by limiting the possible search directions. Because a tangential update of the curve does not change the shape, curve updates will always be in the normal direction, i.e. updates will be of the form $\boldsymbol{\gamma}(t) \to \boldsymbol{\gamma}(t) + h(t)\mathbf{n}(t)$ where $\mathbf{n} = (y', -x')/\sqrt{x'^2 + y'^2}$ is the normal to the curve. We will also only propose curve updates with frequency content proportional to the frequency of the data, i.e. $h : \mathbb{T} \to \mathbb{R}$ will be of the form

$$h(t) = a_{h,0} + \sum_{m=1}^{N_\gamma(\omega)} \left(a_{h,m} \cos(2\pi m t) + b_{h,m} \sin(2\pi m t) \right) \tag{8}$$

where $a_{h,0}$ and $a_{h,m}$ and $b_{h,m}$ for $m = 1, \ldots, N_\gamma(\omega)$ are real constants and $N_\gamma(\omega)$ is an integer proportional to ω.

Remark 2. *It should be noted that the integer parameters in this section, $N(\omega)$, $M(\omega)$ and $N_\gamma(\omega)$, are all selected proportional to ω, but these values are selected with different goals.*

The values of $M(\omega)$ and $N_\gamma(\omega)$ are chosen with respect to the scale of boundary features which can stably be recovered given scattering data collected at frequency ω. In light of the Heisenberg uncertainty principle [32], it is unreasonable to attempt to stably reconstruct features smaller than half of a wavelength in size. Accordingly, we re-parameterize the curve so that it is equally-spaced in arc-length after each boundary update so that these parameters are meaningful.

The value of $N(\omega)$ determines the number of discretization nodes which are used to represent the curve and should be selected to be sufficiently large that the boundary integral equation method used to approximate the solution of the forward problems is accurate. For accuracy, it is typically sufficient to sample the curve at some fixed number of points per wavelength. One contrast between $N(\omega)$ and the other parameters is that there is not much harm in selecting $N(\omega)$ too large, other than the unnecessary computational burden.

2.2 Impedance function models

We consider three models for the impedance function. The first is to model the impedance function, λ_{FS}, in terms of its parameterization, ℓ_{FS}, as a Fourier series:

$$\ell_{\mathrm{FS}}[\mathbf{c}](t) = \sum_{m=-N_c(\omega)}^{N_c(\omega)} c_m \exp(2\pi \imath m t) \ , \tag{9}$$

where $\lambda_{\mathrm{FS}}[\mathbf{c}](\boldsymbol{\gamma}(t)) = \ell_{\mathrm{FS}}[\mathbf{c}](t)$ and $N_c(\omega)$ should be chosen to effectively regularize the model. The inverse problem at a single frequency, (4), can then be rephrased as

$$\left[\hat{\Gamma}_j, \hat{\mathbf{c}}_j\right] = \underset{\Gamma \in S_\Gamma(\omega_j), \mathbf{c} \in \mathbb{C}^{2N_c(\omega_j)+1}}{\arg\min} \sum_{i=1}^{N_d} |\mathbf{u}^{\mathrm{meas}}_{\omega_j, \mathbf{d}_i} - \mathcal{F}^{\mathrm{imp}}_{\omega_j, \mathbf{d}_i}(\Gamma, \lambda_{\mathrm{FS}}[\mathbf{c}])|^2 \ . \tag{10}$$

The second approach is to model the impedance as a linear function of the curvature:

$$\lambda_{\mathrm{CH}}[\boldsymbol{\alpha}] = \alpha_1 + \alpha_2 H \ , \tag{11}$$

where $\boldsymbol{\alpha} = (\alpha_1, \alpha_2) \in \mathbb{C}^2$. The inverse problem at a single frequency, (4), can then be rephrased as

$$\left[\hat{\Gamma}_j, \hat{\boldsymbol{\alpha}}_j\right] = \underset{\Gamma \in S_\Gamma(\omega_j), \boldsymbol{\alpha} \in \mathbb{C}^2}{\arg\min} \sum_{i=1}^{N_d} |\mathbf{u}^{\mathrm{meas}}_{\omega_j, \mathbf{d}_i} - \mathcal{F}^{\mathrm{imp}}_{\omega_j, \mathbf{d}_i}(\Gamma, \lambda_{\mathrm{CH}}[\boldsymbol{\alpha}])|^2 \ . \tag{12}$$

We also consider a more restricted form of the curvature-dependent model which is based directly on the first order model in (3):

$$\lambda_{\mathrm{ABV}}[\boldsymbol{\beta}] = \beta_2 \sqrt{1 - \imath\beta_1} - \frac{\imath\beta_3(1 - \imath\beta_1)}{k_2} H \ , \tag{13}$$

where the parameters can be taken to be non-negative and real, i.e. $\boldsymbol{\beta} \in \mathbb{R}^3_{\geq 0}$. The $\boldsymbol{\beta}$ parameters are related to the physical parameters as follows:

$$\beta_1 = \frac{\delta}{\omega} \ , \quad \beta_2 = \frac{1}{\rho_r c_r \sqrt{1 + \delta^2/\omega^2}} \ , \quad \beta_3 = \frac{1}{\rho_r (1 + \delta^2/\omega^2)} \ . \tag{14}$$

The inverse problem at a single frequency (4) can then be rephrased as

$$\left[\hat{\Gamma}_j, \hat{\boldsymbol{\beta}}_j\right] = \underset{\Gamma \in S_\Gamma(\omega_j), \boldsymbol{\beta} \in \mathbb{R}^3_{\geq 0}}{\arg\min} \sum_{i=1}^{N_d} |\mathbf{u}^{\mathrm{meas}}_{\omega_j, \mathbf{d}_i} - \mathcal{F}^{\mathrm{imp}}_{\omega_j, \mathbf{d}_i}(\Gamma, \lambda_{\mathrm{ABV}}[\boldsymbol{\beta}])|^2 \ . \tag{15}$$

The λ_{ABV} model has the natural physical constraint that $\boldsymbol{\beta} = (\beta_1, \beta_2, \beta_3) \in \mathbb{R}^3_{\geq 0}$. Some natural constraints on the λ_{CH} model are that $\mathrm{Im}(\alpha_1) \leq 0$ and $\mathrm{Im}(\alpha_2) \leq 0$. For these simple models, it is relatively easy to impose such constraints using the methods of Section 3.4. Physical constraints for the λ_{FS} model are both less obvious and more difficult to impose. In the numerical examples in this manuscript, the λ_{FS} model coefficients are unconstrained.

Remark 3. *Above, we parameterize λ_{ABV} by $\boldsymbol{\beta}$ instead of the actual physical parameters, δ, c_r, and ρ_r. One reason for this is that the natural constraints are $\delta \geq 0$, $c_r > 0$, and $\rho_r > 0$ and the impedance function becomes infinite if $c_r = 0$ or $\rho_r = 0$. The constrained optimization problem is simpler for the closed, convex constraint set of the $\boldsymbol{\beta}$ variables. In particular, we do not have to select arbitrary lower bounds for c_r and ρ_r.*

2.3 Fréchet derivatives of the forward operator $\mathcal{F}^{\text{imp}}$

Let $\mathcal{F}^{\text{imp}}_{\omega,\mathbf{d}}$ be the forward map defined as in the introduction, i.e. $\mathcal{F}^{\text{imp}}_{\omega,\mathbf{d}}(\Gamma, \lambda) \in \mathbb{C}^{N_r}$ is the solution of the impedance scattering problem (2) for the incident field $u^{\text{inc}} = \exp(\imath k_2 \mathbf{d} \cdot \mathbf{x})$ evaluated at the receptors, $\mathbf{r}_j$. To apply standard iterative solvers to the minimization problem (4), we require expressions for the derivatives of $\mathcal{F}^{\text{imp}}_{\omega,\mathbf{d}}$ with respect to the curve Γ and the impedance function λ. We will drop the dependence of $\mathcal{F}^{\text{imp}}$ on ω and $\mathbf{d}$ for the sake of brevity.

The derivations of the Fréchet derivative formulas we need are more straightforward with respect to parameterizations of the curve and impedance function. Let $\boldsymbol{\gamma} : \mathbb{T} \to \mathbb{R}^2$ and $\ell : \mathbb{T} \to \mathbb{C}$ be functions on the unit torus, $[0, 1]$, such that $\Gamma = \boldsymbol{\gamma}([0, 1])$ and $\lambda(\boldsymbol{\gamma}(t)) = \ell(t)$. We will use the abusive notation $\mathcal{F}^{\text{imp}}(\boldsymbol{\gamma}, \ell)$ for $\mathcal{F}^{\text{imp}}(\Gamma, \lambda)$. The advantage of the function $\mathcal{F}^{\text{imp}}(\boldsymbol{\gamma}, \ell)$ is that it is a map between fixed Banach spaces, say $\mathcal{F}^{\text{imp}} : C^4(\mathbb{T}) \times C^2(\mathbb{T}) \to \mathbb{C}^{N_r}$, whereas in the original notation the space for λ changes as Γ changes. Below, the notations $D_1\mathcal{F}^{\text{imp}}(\boldsymbol{\gamma}, \ell)$ and $D_2\mathcal{F}^{\text{imp}}(\boldsymbol{\gamma}, \ell)$ refer to the Fréchet derivatives with respect to the first and second inputs (holding the other fixed), respectively.

Explicit formulas for these derivatives are known. They are expressed as the solutions of impedance scattering problems. In the theorem below, parameterizations defined on $\mathbb{T}$ must be interpreted as functions on the boundary, Γ. This is accomplished by composition with the inverse map $\boldsymbol{\gamma}^{-1}$ in the same way that $\lambda = \ell \circ \boldsymbol{\gamma}^{-1}$.

Theorem 1 (Adapted from [25, Theorem 4.8] and [24, Theorem 4.1])**.** *Let Γ be a regular, closed curve and λ be a complex-valued function on Γ with $\text{Im}(\lambda) \geq 0$. Assume these functions have parameterizations $\boldsymbol{\gamma} \in C^4(\mathbb{T})$ and $\ell \in C^2(\mathbb{T})$, respectively. Let $u = u^{scat} + u^{inc}$ be the total field for the solution of the original obstacle problem* (2)*.*

Let $\mathbf{h} \in C^4(\mathbb{T})$. *The* j*th entry of* $\left[D_1\mathcal{F}^{imp}(\boldsymbol{\gamma},\ell)\right]\mathbf{h}$ *is equal to* $v_\gamma(\mathbf{r}_j)$, *where*

$$\begin{aligned} -(\Delta + k_2^2)v_\gamma &= 0 && \text{in } \Omega\,, \\ \partial_n v_\gamma + \imath k_2 \lambda v_\gamma &= k_2^2(\mathbf{h}\circ\boldsymbol{\gamma}^{-1})\cdot\mathbf{n}u \\ &\quad + \frac{d}{ds}\left((\mathbf{h}\circ\boldsymbol{\gamma}^{-1})\cdot\mathbf{n}\frac{du}{ds}\right) \\ &\quad - \lambda(\mathbf{h}\circ\boldsymbol{\gamma}^{-1})\cdot\mathbf{n}\,(\partial_n u - Hu) \\ &\quad + \frac{d\lambda}{ds}(\mathbf{h}\circ\boldsymbol{\gamma}^{-1})\cdot\boldsymbol{\tau}u && \text{on } \Gamma\,, \\ \sqrt{|x|}\left(v_\gamma - \imath k_2\frac{x}{|x|}\cdot\nabla v_\gamma\right) &\to 0 && \text{as } |x|\to\infty\,, \end{aligned} \tag{16}$$

and $\boldsymbol{\tau}$ *is the positively oriented tangent vector on* Γ.

Let $g \in C^2(\mathbb{T})$. *The* j*th entry of* $\left[D_2\mathcal{F}^{imp}(\boldsymbol{\gamma},\ell)\right]g$ *is equal to* $v_\lambda(\mathbf{r}_j)$, *where*

$$\begin{aligned} -(\Delta + k_2^2)v_\lambda &= 0 && \text{in } \Omega\,, \\ \partial_n v_\lambda + \imath k_2\lambda v_\lambda &= -\imath k_2(g\circ\boldsymbol{\gamma}^{-1})u && \text{on } \Gamma\,, \\ \sqrt{|x|}\left(v_\lambda - \imath k_2\frac{x}{|x|}\cdot\nabla v_\lambda\right) &\to 0 && \text{as } |x|\to\infty\,. \end{aligned} \tag{17}$$

Remark 4. *In practice, we only consider normal perturbations. The formula for* $D_1\mathcal{F}^{imp}$ *simplifies in this case because* $(\mathbf{h}\circ\boldsymbol{\gamma}^{-1})\cdot\boldsymbol{\tau} = 0$.

For the λ_{CH} and λ_{ABV} models of the impedance function, the impedance function depends on the curvature of the domain. In terms of parameterizations, we write this as $\ell[\boldsymbol{\gamma}]$. The Fréchet derivative of $\mathcal{F}^{\mathrm{imp}}(\boldsymbol{\gamma},\ell[\boldsymbol{\gamma}])$ with respect to $\boldsymbol{\gamma}$ can then be obtained by applying the chain rule

$$\left[D_{\boldsymbol{\gamma}}\mathcal{F}^{\mathrm{imp}}(\boldsymbol{\gamma},\ell[\boldsymbol{\gamma}])\right]\mathbf{h} = \left[D_1\mathcal{F}^{\mathrm{imp}}(\boldsymbol{\gamma},\ell[\boldsymbol{\gamma}])\right]\mathbf{h} + \left[D_2\mathcal{F}^{\mathrm{imp}}(\boldsymbol{\gamma},\ell[\boldsymbol{\gamma}])\right]\left[D_{\boldsymbol{\gamma}}\ell[\boldsymbol{\gamma}]\right]\mathbf{h}\,.$$

The formula for $D_{\boldsymbol{\gamma}}\ell[\boldsymbol{\gamma}]$ for both the λ_{CH} and λ_{ABV} models requires a formula for the Fréchet derivative of the curvature parameterization, $H[\boldsymbol{\gamma}]$, with respect to the boundary. The following direct formula for this derivative can be verified by hand calculation:

Proposition 1. *Let* $\boldsymbol{\gamma} \in C^3(\mathbb{T})$ *and let* $H[\boldsymbol{\gamma}]$ *be the signed curvature as defined in* (6). *Let* $\mathbf{h}$ *be a normal perturbation of the curve, i.e.* $\mathbf{h}(t) = h(t)\mathbf{n}(t)$ *for a function* $h \in C^2(\mathbb{T})$. *Then,*

$$\left[D_{\boldsymbol{\gamma}}H[\boldsymbol{\gamma}]\right]\mathbf{h} = -H[\boldsymbol{\gamma}]^2 h + \frac{x'x'' + y'y''}{(x'^2+y'^2)^2}h' - \frac{1}{x'^2+y'^2}h''\,. \tag{18}$$

3 Optimization methods

This section describes details related to the optimization procedures used to solve the inverse scattering problems. The continuation-in-frequency approach [7, 12–16, 20, 22, 31, 32, 67] is the over-arching framework. This applies to multi-frequency data collected for a set of frequencies $\omega_1 < \omega_2 < \cdots < \omega_{N_k}$. As explained in the introduction, this approach begins with initial guesses, $\hat{\Gamma}_0$ and $\hat{\lambda}_0$, of the domain boundary and impedance function, respectively, and does the iteration

$$\left[\hat{\Gamma}_j, \hat{\lambda}_j\right] = \underset{\Gamma \in S_\Gamma(\omega_j), \lambda \in S_\lambda(\omega_j)}{\text{loc arg min}} \sum_{i=1}^{N_d} |\mathbf{u}^{\text{meas}}_{\omega_j, \mathbf{d}_i} - \mathcal{F}^{\text{imp}}_{\omega_j, \mathbf{d}_i}(\Gamma, \lambda)|^2 \,, \tag{19}$$

where the notation loc arg min indicates that the minimization problem is solved using a standard local optimization procedure based on gradient information and the initial guess $\left[\hat{\Gamma}_{j-1}, \hat{\lambda}_{j-1}\right]$. The basic idea of the method is that the global minimizers at each frequency, subject to appropriate choices of the constraint sets, should be sufficiently close that a local solve works to find the global minimum at each step. See the references above for more discussion.

Section 3.1 provides an overview of the alternating minimization approach we use to solve problems of the form (19), which alternates between minimization of the objective over the domain parameters and over the impedance parameters. We use two different methods for obtaining descent directions (in terms of either the domain or impedance function parameters): Gauss-Newton and steepest descent. Formulas for these in the inverse obstacle setting are provided in Section 3.2. We discuss the strategies used to minimize the objective function under the given constraints in the case of the domain in Section 3.3 and in the case of the impedance function in Section 3.4.

3.1 Alternating minimization

We solve optimization problems of the form (19) by alternating minimization: we apply a step of an optimization algorithm with respect to the domain boundary parameters and then a step of an optimization algorithm with respect to the impedance function parameters. This approach is classical [56, 72] and has been previously applied in the non-convex setting [11, 19]. This is particularly convenient because our methods for staying in the constraint sets for the domain parameters and the impedance function parameters are different.

At frequency ω_j, the initial guesses for the domain boundary and impedance function are $\Gamma_j^{(0)} = \hat{\Gamma}_{j-1}$ and $\lambda_j^{(0)} = \hat{\lambda}_{j-1}$, respectively. Then, we apply the following alternating minimization iteration to find a local solution of (19):

- (Fix λ and optimize over Γ) Let $\boldsymbol{\gamma} : \mathbb{T} \to \mathbb{R}^2$ be a parameterization of $\Gamma_j^{(q-1)}$. Find the parameterization of a descent direction $\mathbf{h} = h\mathbf{n}$ with respect to the domain boundary, where $h : \mathbb{T} \to \mathbb{R}$ such that the curve

$\Gamma_j^{(q)}$ with the parameterization $\boldsymbol{\gamma}+\mathbf{h}:\mathbb{T}\to\mathbb{R}^2$ satisfies $\Gamma_j^{(q)}\in S_\Gamma(\omega_j)$ and

$$\sum_{i=1}^{N_d}|\mathbf{u}^{\text{meas}}_{\omega_j,\mathbf{d}_i}-\mathcal{F}^{\text{imp}}_{\omega_j,\mathbf{d}_i}(\Gamma_j^{(q)},\lambda_j^{(q-1)})|^2\le\sum_{i=1}^{N_d}|\mathbf{u}^{\text{meas}}_{\omega_j,\mathbf{d}_i}-\mathcal{F}^{\text{imp}}_{\omega_j,\mathbf{d}_i}(\Gamma_j^{(q-1)},\lambda_j^{(q-1)})|^2\,. \tag{20}$$

- (Fix Γ and optimize over λ) Let $\boldsymbol{\gamma}:\mathbb{T}\to\mathbb{R}^2$ be a parameterization of $\Gamma_j^{(q)}$. Find the parameterization of a descent direction $g:\mathbb{T}\to\mathbb{C}$ with respect to the impedance function such that the impedance function, $\lambda_j^{(q)}$ with parameterization $\ell_j^{(q)}(t)=\ell_j^{(q-1)}(t)+g(t)$ satisfies $\lambda_j^{(q)}\in S_\lambda(\omega_j)$ and

$$\sum_{i=1}^{N_d}|\mathbf{u}^{\text{meas}}_{\omega_j,\mathbf{d}_i}-\mathcal{F}^{\text{imp}}_{\omega_j,\mathbf{d}_i}(\Gamma_j^{(q)},\lambda_j^{(q)})|^2\le\sum_{i=1}^{N_d}|\mathbf{u}^{\text{meas}}_{\omega_j,\mathbf{d}_i}-\mathcal{F}^{\text{imp}}_{\omega_j,\mathbf{d}_i}(\Gamma_j^{(q)},\lambda_j^{(q-1)})|^2\,. \tag{21}$$

Methods for finding appropriate descent directions and satisfying the constraints are discussed in the following subsections. Because we generally apply second order methods (Gauss-Newton) to the boundary minimization and first order methods (projected gradient descent) to deal with the constraint sets for the impedance minimization, we run multiple iterations, determined by N_{inner}, of the impedance minimization for every iteration of the full framework.

We impose a number of stopping criteria. We set a tolerance ϵ_R for the relative residual

$$R_\omega(\hat\Gamma,\hat\lambda)=\sqrt{\sum_{i=1}^{N_d}\left|\mathbf{u}^{\text{meas}}_{\omega,\mathbf{d}_i}-\mathcal{F}^{\text{imp}}_{\omega,\mathbf{d}_i}(\hat\Gamma,\hat\lambda)\right|^2\Big/\sum_{i=1}^{N_d}\left|\mathbf{u}^{\text{meas}}_{\omega,\mathbf{d}_i}\right|^2}\,, \tag{22}$$

such that we terminate if $R_\omega\le\epsilon_R$. We try to detect stagnation by monitoring for small relative changes in the norm of the domain parameters, impedance parameters, and the relative residual. These tolerances are denoted by $\epsilon_{s,\Gamma}$, $\epsilon_{s,\lambda}$, and $\epsilon_{s,R}$, respectively. We also impose a maximum number of iterations, N_f, of the alternating minimization framework at each frequency. See algorithm 5 at the end of the section for pseudo-code of the alternating minimization procedure. This pseudo-code uses routines OPTIMIZE_DOMAIN and OPTIMIZE_IMPEDANCE which are detailed below after a discussion of the procedures for domain and impedance function optimization; see algorithms 3 and 4.

3.2 Obtaining descent directions

The objective function in (19) is in the form of a nonlinear least squares problem. Here we briefly review two popular descent methods for such objective functions: steepest descent and Gauss-Newton.

Consider a function $F:\mathbb{C}^n\to\mathbb{R}$ of the form

$$F(\mathbf{v}) = \frac{1}{2}\sum_{j=1}^{m} |f_j(\mathbf{v}) - z_j|^2 = \frac{1}{2}\|\mathbf{f}(\mathbf{v}) - \mathbf{z}\|^2 \ ,$$

where each $f_j : \mathbb{C}^n \to \mathbb{C}$ is holomorphic in the complex v_i variables, the data are $z_i \in \mathbb{C}$ for $i = 1, \ldots, m$, and $\mathbf{f}(\mathbf{v})$ and $\mathbf{z}$ are the vectors collecting these values. Recall that the Jacobian is the matrix $\mathbf{J}(\mathbf{v}) \in \mathbb{C}^{m\times n}$ with the entries $J_{ji}(\mathbf{v}) = \partial_{v_i} f_j(\mathbf{v})$.

The complex gradient of F is then [51]

$$\nabla_v F = (\mathbf{J}(\mathbf{v}))^*(\mathbf{f}(\mathbf{v}) - \mathbf{z}) \ ,$$

where the $(\mathbf{J}(\mathbf{v}))^*$ denotes the conjugate transpose. Using the negative of the gradient as the search direction is known as steepest descent minimization.

A reasonable step size, d, in the direction of the negative of the gradient can be obtained by minimizing the approximation

$$\begin{aligned} F(\mathbf{v} - d\nabla_v F) &\approx \frac{1}{2}\|\mathbf{f}(\mathbf{v}) - d\mathbf{J}(\mathbf{v})\nabla_v F - \mathbf{z}\|^2 \\ &= \frac{1}{2}\|\mathbf{f}(\mathbf{v}) - \mathbf{z}\|^2 - d\|\nabla_v F\|^2 + \frac{d^2}{2}\|J(\mathbf{v})\nabla_v F\|^2 \ , \end{aligned}$$

as a function of d. The minimum occurs for

$$d = \frac{\|\nabla_v F\|^2}{\|J(\mathbf{v})\nabla_v F\|^2} \ . \tag{23}$$

This is the so-called Cauchy point for the linearization. We use it as an initial guess for the step size when the direction is based on the gradient.

The Gauss-Newton method is based on the linearization $\mathbf{f}(\mathbf{v}+\Delta\mathbf{v}) \approx \mathbf{f}(\mathbf{v}) + \mathbf{J}(\mathbf{v})\Delta\mathbf{v}$. The minimizer $\Delta\mathbf{v}$ of the approximation

$$F(\mathbf{v} + \Delta\mathbf{v}) \approx \|\mathbf{f}(\mathbf{v}) - \mathbf{z} + \mathbf{J}(\mathbf{v})\Delta\mathbf{v}\|^2$$

is then the linear least squares solution of the system

$$\mathbf{J}(\mathbf{v})\Delta\mathbf{v} = \mathbf{z} - \mathbf{f}(\mathbf{v}) \ ,$$

which can be computed by direct methods. The Gauss-Newton step has a built-in notion of the appropriate step size, so the initial guess for d is 1 for this descent direction.

Remark 5. *For the domain and the λ_{ABV} impedance model, the parameters are real-valued so that the objective function is of the form $F : \mathbb{R}^n \to \mathbb{R}$, with $f_j : \mathbb{R}^n \to \mathbb{C}$. In this case, we are interested in the real gradient and real Gauss-Newton directions, which are straightforwardly computed by decomplexifying $\mathbf{f}$. The gradient is*

$$\nabla_v \tilde{F} = \begin{bmatrix} \mathrm{Re}(\mathbf{J}(\mathbf{v})) \\ \mathrm{Im}(\mathbf{J}(\mathbf{v})) \end{bmatrix}^T \begin{bmatrix} \mathrm{Re}(\mathbf{f}(\mathbf{v}) - \mathbf{z}) \\ \mathrm{Im}(\mathbf{f}(\mathbf{v}) - \mathbf{z}) \end{bmatrix} \ ,$$

and for the Gauss-Newton method, the update is the linear least squares solution of

$$\begin{bmatrix}\mathrm{Re}(\mathbf{J}(\mathbf{v}))\\ \mathrm{Im}(\mathbf{J}(\mathbf{v}))\end{bmatrix}\Delta\mathbf{v} = -\begin{bmatrix}\mathrm{Re}(\mathbf{f}(\mathbf{v})-\mathbf{z})\\ \mathrm{Im}(\mathbf{f}(\mathbf{v})-\mathbf{z})\end{bmatrix}\ .$$

Specifics for boundary curve optimization Suppose that at frequency ω we have the approximate boundary curve, Γ, and the approximate impedance function λ. Suppose that this curve has the parameterization $\boldsymbol{\gamma}:\mathbb{T}\to\mathbb{R}^2$. As noted above, we consider only normal perturbations of this curve of the form $\mathbf{h}=h\mathbf{n}$, where $\mathbf{n}(t)$ is the normal to the curve at $\boldsymbol{\gamma}(t)$. Let $N_\gamma(\omega)$ be given and $h_{\mathbf{w}}$ be parameterized as in (8), i.e. as a real Fourier series, with parameters $\mathbf{w}=(a_{h,0},a_{h,1},\ldots,a_{h,N_\gamma},b_{h,0},b_{h,1},\ldots,b_{h,N_\gamma})\in\mathbb{R}^{2N_\gamma+1}$. Then, we consider minimizing the objective function

$$F_\Gamma(\mathbf{w})=\sum_{i=1}^{N_d}|\mathbf{u}^{\mathrm{meas}}_{\omega,\mathbf{d}_i}-\mathcal{F}^{\mathrm{imp}}_{\omega,\mathbf{d}_i}(\Gamma(\mathbf{w}),\lambda)|^2\ ,$$

where the curve $\Gamma(\mathbf{w})$ is the curve with the parameterization $\boldsymbol{\gamma}_{\mathbf{w}}:\mathbb{T}\to\mathbb{R}^2$ defined by $\boldsymbol{\gamma}_{\mathbf{w}}(s)=\boldsymbol{\gamma}(t)+h_{\mathbf{w}}(t)\mathbf{n}(t)$.

The values of

$$\partial_{\mathrm{w}_j}\mathcal{F}^{\mathrm{imp}}_{\omega,\mathbf{d}_i}(\boldsymbol{\gamma}_{\mathbf{w}},\ell[\boldsymbol{\gamma}_{\mathbf{w}}])\in\mathbb{C}^{N_r}\ ,$$

where $\ell[\boldsymbol{\gamma}_{\mathbf{w}}]$ indicates the dependence of the parameterization of λ on the curve in the λ_{ABV} and λ_{CH} models, can be obtained using the Fréchet derivative formulae of Section 2.3 and applying the chain rule when appropriate. In particular,

$$\partial_{\mathrm{w}_j}\mathcal{F}^{\mathrm{imp}}_{\omega,\mathbf{d}_i}(\boldsymbol{\gamma}_{\mathbf{w}},\ell[\boldsymbol{\gamma}_{\mathbf{w}}])=\begin{cases}\left[D_{\boldsymbol{\gamma}}\mathcal{F}^{\mathrm{imp}}_{\omega,\mathbf{d}_i}(\boldsymbol{\gamma}_{\mathbf{w}},\ell[\boldsymbol{\gamma}_{\mathbf{w}}])\right]\phi_j\mathbf{n} & \text{if} \quad j\le N_\gamma+1\\ \left[D_{\boldsymbol{\gamma}}\mathcal{F}^{\mathrm{imp}}_{\omega,\mathbf{d}_i}(\boldsymbol{\gamma}_{\mathbf{w}},\ell[\boldsymbol{\gamma}_{\mathbf{w}}])\right]\psi_j\mathbf{n} & \text{if} \quad j>N_\gamma+1\end{cases},$$

where $\phi_j(t)=\cos(2\pi(j-1)t)$ and $\psi_j(s)=\sin(2\pi(j-N_\gamma-1)t)$.

Remark 6. *The Jacobian matrix for the geometry update, $\mathbf{J}(\mathbf{w})$, is $N_rN_i\times(2N_\gamma+1)$. We must solve a PDE for each incident direction $\mathbf{d}_i$ and each entry of $\mathbf{w}$ to fill the matrix. See Appendix A.3 for a brief discussion of computational costs.*

Specifics for impedance function optimization Suppose that at frequency ω we have the approximate boundary curve, Γ. We consider three objective functions, depending on the impedance function model:

$$F_{\lambda_{\mathrm{FS}}}(\mathbf{c}) = \sum_{i=1}^{N_d} |\mathbf{u}^{\mathrm{meas}}_{\omega,\mathbf{d}_i} - \mathcal{F}^{\mathrm{imp}}_{\omega,\mathbf{d}_i}(\Gamma, \lambda_{\mathrm{FS}}[\mathbf{c}])|^2 \ ,$$

$$F_{\lambda_{\mathrm{CH}}}(\boldsymbol{\alpha}) = \sum_{i=1}^{N_d} |\mathbf{u}^{\mathrm{meas}}_{\omega,\mathbf{d}_i} - \mathcal{F}^{\mathrm{imp}}_{\omega,\mathbf{d}_i}(\Gamma, \lambda_{\mathrm{CH}}[\boldsymbol{\alpha}])|^2 \ ,$$

$$F_{\lambda_{\mathrm{ABV}}}(\boldsymbol{\beta}) = \sum_{i=1}^{N_d} |\mathbf{u}^{\mathrm{meas}}_{\omega,\mathbf{d}_i} - \mathcal{F}^{\mathrm{imp}}_{\omega,\mathbf{d}_i}(\Gamma, \lambda_{\mathrm{ABV}}[\boldsymbol{\beta}])|^2 \ .$$

As above, the entries of the Jacobian can be obtained using the Fréchet derivative formulae of Section 2.3. For example,

$$\partial_{\alpha_j} \mathcal{F}^{\mathrm{imp}}_{\omega,\mathbf{d}_i}(\boldsymbol{\gamma}, \lambda_{\mathrm{CH}}[\boldsymbol{\alpha}] \circ \boldsymbol{\gamma}) = \begin{cases} \left[D_2 \mathcal{F}^{\mathrm{imp}}_{\omega,\mathbf{d}_i}(\boldsymbol{\gamma}, \lambda_{\mathrm{CH}}[\boldsymbol{\alpha}] \circ \boldsymbol{\gamma})\right] 1 & \text{if} \quad j = 1 \\ \left[D_2 \mathcal{F}^{\mathrm{imp}}_{\omega,\mathbf{d}_i}(\boldsymbol{\gamma}, \lambda_{\mathrm{CH}}[\boldsymbol{\alpha}] \circ \boldsymbol{\gamma})\right] H[\boldsymbol{\gamma}] & \text{if} \quad j = 2 \end{cases} ,$$

where 1 denotes the function that is constant 1 and $H[\boldsymbol{\gamma}]$ is the parameterization of the signed curvature function on Γ. The λ_{FS} and λ_{ABV} cases can be treated in similar fashion; we omit the details for the sake of brevity.

3.3 Filtering methods for the domain

Following the notation of the previous section, let $\mathbf{w}$ be the Fourier series coefficients defining an update $h_{\mathbf{w}}$. We find coefficients $\mathbf{w}_{\mathrm{gn}}$ and $\mathbf{w}_{\mathrm{sd}}$ corresponding to Gauss-Newton and steepest descent directions, respectively, and set d to be the step length for steepest descent determined using the Cauchy point formula (23). We set $h^{\mathrm{gn}} = h_{\mathbf{w}_{\mathrm{gn}}}$ and $h^{\mathrm{sd}} = h_{d\mathbf{w}_{\mathrm{sd}}}$. For either update, it is not guaranteed that the new curve, $\Gamma(\mathbf{w}_{\mathrm{gn}})$ with parameterization $\boldsymbol{\gamma}_{\mathrm{gn}} = \boldsymbol{\gamma} + h^{\mathrm{gn}}\mathbf{n}$ or $\Gamma(d\mathbf{w}_{\mathrm{sd}})$ with parameterization $\boldsymbol{\gamma}_{\mathrm{sd}} = \boldsymbol{\gamma} + h^{\mathrm{sd}}\mathbf{n}$, is in the constraint set, $S_\Gamma(\omega)$. We follow two strategies for modifying these updates [7]: step-length filtering and Gaussian filtering.

Step-length filtering is the basic strategy of shortening the step in the given direction until the constraints are met and the residual is non-increasing. Let $\eta_{\mathrm{filt}} > 1$ and N_{filt}, a positive integer, be the filtering parameters. For any update h with parameters $\mathbf{w}$, the filtered update is then $h/\eta_{\mathrm{filt}}^{n_{\mathrm{filt}}}$, where n_{filt} is the smallest ℓ with $0 \le \ell \le N_{\mathrm{filt}}$ such that

$$\Gamma(\mathbf{w}/\eta_{\mathrm{filt}}^{\ell}) \in S_\Gamma(\omega) \quad \text{and} \quad F_\Gamma(\mathbf{w}/\eta_{\mathrm{filt}}^{\ell}) \le F_\Gamma(\mathbf{0}) \ ,$$

with the convention that the filtered step is of size 0 if there is no ℓ satisfying the conditions. We denote the step-length filtered steps for each direction by $h^{\mathrm{gn,sf}}$ and $h^{\mathrm{sd,sf}}$.

In practice, step-length filtering results in overly short steps when the update induces self-intersections or high curvature. The idea of Gaussian filtering is to attenuate high frequency components of the update in order to more efficiently avoid these geometric issues [7].

Let $\mathbf{w}$ be the parameters of a given update. Recall that the first $N_\gamma + 1$ entries correspond to cosines of increasing frequency and the last N_γ entries to sines of increasing frequency. Let $\sigma_{\text{filt}} > 0$ be a given filtering parameter determining the width of a Gaussian and define the diagonal linear operator G_σ by

$$G_\sigma(\mathbf{e}_m) = \begin{cases} \exp\left(-\frac{(m-1)^2}{\sigma^2 N_h^2}\right)\mathbf{e}_m & \text{if} \quad 1 \le m \le N_h + 1, \\ \exp\left(-\frac{(m-N_h-1)^2}{\sigma^2 N_h^2}\right)\mathbf{e}_m & \text{if} \quad N_h + 2 \le m \le 2N_h + 1. \end{cases}$$

The filtered update is then $h_{\mathbf{w}_{\text{gf}}}$, where $\mathbf{w}_{\text{gf}} = G_{\sigma_{\text{filt}}^{n_{\text{filt}}}}\mathbf{w}$ and n_{filt} is the smallest ℓ with $0 \le \ell \le N_{\text{filt}}$ such that

$$\Gamma(G_{\sigma_{\text{filt}}^{\ell}}\mathbf{w}) \in S_\Gamma(\omega) \quad \text{and} \quad F_\Gamma(G_{\sigma_{\text{filt}}^{\ell}}\mathbf{w}) \le F_\Gamma(\mathbf{0}) \ ,$$

with the convention that the filtered step is of size 0 if there is no ℓ satisfying the conditions. We denote the Gaussian filtered steps for each direction by $h^{\text{gn,gf}}$ and $h^{\text{sd,gf}}$.

We have found that the best performance is obtained by attempting all strategies. At each step, we select h to be the filtered step out of the options $h^{\text{gn,sf}}$, $h^{\text{gn,gf}}$, $h^{\text{sd,sf}}$, and $h^{\text{sd,gf}}$ for which the updated curve results in the minimum residual.

To keep the discretization nodes evenly distributed and to ensure that the regularization parameters $N_c(\omega)$, $N_\gamma(\omega)$, and $M(\omega)$ are meaningful, we resample the domain so that the nodes are equally spaced in arc-length. We use an algorithm similar to the one described in [17], though we simply resample the Fourier interpolant instead of attempting to find a new, bandlimited interpolant, as in [17].

See algorithm 3 for a detailed pseudo-code of the filtering procedure as well as the supporting subroutines in algorithms 1 and 2, which describe the methods for updating the domain and parameterizations.

Algorithm 1 $\mathbf{w}$ = FOURIER_SERIES_COEFFICIENTS(f, $\{t_1, \ldots, t_n\}$, m)
Sample the function at the points and compute the Fourier coefficients of the resulting discrete vector. Truncate or pad as necessary.

Input: f, $\{t_1, \ldots, t_n\}$, m

1: $\mathbf{f} \leftarrow (f(t_1), \ldots, f(t_n))$
2: $\mathbf{w} \leftarrow DFT(\mathbf{f})$ ▷ sin/cos Fourier transform if $\mathbf{w}$ real
3: $\mathbf{w} \leftarrow$ pad or truncate $\mathbf{w}$ to order m

Output: $\mathbf{w}$

Algorithm 2 $\boldsymbol{\gamma}^{\text{out}}, \ell^{\text{out}} = \text{DOMAIN\_UPDATE}(\boldsymbol{\gamma}, h, \ell, \omega)$

Given the parameterization of a curve update, form the updated curve, resample in arc-length, and update the impedance function if necessary.

Input: $\boldsymbol{\gamma}$, h, ℓ, ω

$\mathbf{n} \leftarrow$ normal vector of parameterization $\boldsymbol{\gamma}$

$N_{\text{samp}} \leftarrow 2N(\omega) + 1$ ▷ Order $N(\omega)$ expansion is length N_{samp}

$\mathbf{w} \leftarrow \text{FOURIER\_SERIES\_COEFFICIENTS}(\boldsymbol{\gamma} + h\mathbf{n}, \{j/N_{\text{samp}}\}_{j=1}^{N_{\text{samp}}}, N(\omega))$

$t_1, \ldots, t_{N_{\text{samp}}} \leftarrow \text{ARC\_LENGTH\_RESAMPLE}(\mathbf{w})$ ▷ See definition below

$\mathbf{w}^{\text{out}} \leftarrow \text{FOURIER\_SERIES\_COEFFICIENTS}(\boldsymbol{\gamma} + h\mathbf{n}, \{t_j\}_{j=1}^{N_{\text{samp}}}, N(\omega))$

$\boldsymbol{\gamma}^{\text{out}} \leftarrow$ function defined by coefficients $\mathbf{w}^{\text{out}}$

if impedance model is λ_{FS} **then**

    ▷ Resample impedance function and truncate Fourier series

    $\mathbf{v}^{\text{out}} \leftarrow \text{FOURIER\_SERIES\_COEFFICIENTS}(\ell, \{t_j\}_{j=1}^{N_{\text{samp}}}, N_c(\omega))$

    $\ell^{\text{out}} \leftarrow$ function defined by coefficients $\mathbf{v}^{\text{out}}$

else

    $\ell^{\text{out}} \leftarrow \ell$

Output: $\boldsymbol{\gamma}^{\text{out}}$,$\ell^{\text{out}}$.

function $\text{ARC\_LENGTH\_RESAMPLE}(\mathbf{w})$

    $N \leftarrow$ order of the coefficients $\mathbf{w}$

    $\boldsymbol{\gamma} \leftarrow$ function defined by coefficients $\mathbf{w}$

    $L \leftarrow \int_0^1 |\boldsymbol{\gamma}'(t)|\, dt$ ▷ Length of curve

    $t_1, \ldots, t_{2N+1} \leftarrow$ points such that $\int_{t_j}^{t_j+1} |\boldsymbol{\gamma}'(t)|\, dt = L/(2N+1)$

    Return $\{t_j\}_{j=1}^{2N+1}$

Algorithm 3 $\boldsymbol{\gamma}^{\text{out}}, \ell^{\text{out}} = \text{OPTIMIZE\_DOMAIN}(\boldsymbol{\gamma}, \ell, \omega, N_{\text{filt}}, \sigma_{\text{filt}}, \eta_{\text{filt}})$
Minimize the residual with respect to the domain parameterization, $\boldsymbol{\gamma}$, holding the parameters of the impedance function, ℓ, fixed. For the λ_{FS} model, the parameterization ℓ may be resampled along with $\boldsymbol{\gamma}$.

Input: $\boldsymbol{\gamma}$, ℓ, ω, N_{filt}, σ_{filt}, η_{filt}.
Initialize $R_0 \leftarrow R_\omega(\boldsymbol{\gamma}, \ell)$, $R_{\text{out}} \leftarrow R_0$, $\boldsymbol{\gamma}^{\text{out}} \leftarrow \boldsymbol{\gamma}$, $\ell^{\text{out}} \leftarrow \ell$
for $h = \{h^{\text{gn}}, h^{\text{sd}}\}$ **do** ▷ Gauss-Newton and steepest-descent directions.
  $\mathbf{w} \leftarrow \text{FOURIER\_SERIES\_COEFFICIENTS}(h, \{j/N(\omega)\}_{j=1}^{N(\omega)}, N(\omega))$
  for $p = 1, \ldots, N_{\text{filt}}$ **do** ▷ Try Gaussian filter first
    $\mathbf{w}^G \leftarrow G_{\sigma_{\text{filt}}^p} \mathbf{w}$
    $h^G \leftarrow$ function defined by coefficients $\mathbf{w}^G$
    $\boldsymbol{\gamma}^G, \ell^G \leftarrow \text{DOMAIN\_UPDATE}(\boldsymbol{\gamma}, h^G, \ell, \omega)$
    if $\boldsymbol{\gamma}^G \in S_\Gamma(\omega)$ and $R_\omega(\boldsymbol{\gamma}^G, \ell^G) < R_0$ **then**
      if $R_\omega(\boldsymbol{\gamma}^G, \ell^G) < R_{\text{out}}$ **then**
        Update $\boldsymbol{\gamma}^{\text{out}} \leftarrow \boldsymbol{\gamma}^G$, $\ell^{\text{out}} \leftarrow \ell^G$, $R_{\text{out}} \leftarrow R_\omega(\boldsymbol{\gamma}^G, \ell^G)$
      break
  for $p = 1, \ldots, N_{\text{filt}}$ **do** ▷ Then try step-length filter
    $h^S \leftarrow h/\eta_{\text{filt}}^p$
    $\boldsymbol{\gamma}^S, \ell^S \leftarrow \text{DOMAIN\_UPDATE}(\boldsymbol{\gamma}, h^S, \ell, \omega)$
    if $\boldsymbol{\gamma}^S \in S_\Gamma(\omega)$ and $R_\omega(\boldsymbol{\gamma}^S, \ell^S) < R_0$ **then**
      if $R_\omega(\boldsymbol{\gamma}^S, \ell^S) < R_{\text{out}}$ **then**
        Update $\boldsymbol{\gamma}^{\text{out}} \leftarrow \boldsymbol{\gamma}^S$, $\ell^{\text{out}} \leftarrow \ell^S$, $R_{\text{out}} \leftarrow R_\omega(\boldsymbol{\gamma}^S, \ell^S)$
      break
Output: $\boldsymbol{\gamma}^{\text{out}}$,$\ell^{\text{out}}$.

3.4 Projection methods for the impedance function

The constraint sets for the λ_{CH} and λ_{ABV} models are closed and convex, so the corresponding constrained minimization problem can be treated by a projected gradient method [37, 74]. In particular, the impedance optimization problems are of the form

$$\min_{\mathbf{v} \in \mathcal{C}} F(\mathbf{v}) \ ,$$

where $\mathcal{C}$ is a closed, convex set. The simple iteration

$$\mathbf{v}_{j+1} = \text{proj}_{\mathcal{C}}(\mathbf{v}_j - d_j \nabla_v F(\mathbf{v}_j)) \ , \tag{24}$$

where d_j is a step-length parameter and

$$\text{proj}_{\mathcal{C}}(\mathbf{y}) = \arg\min_{\mathbf{x} \in \mathcal{C}} \|\mathbf{y} - \mathbf{x}\| \ ,$$

is known as a projected gradient method. The iteration is known to converge under mild assumptions on F [37, 39].

The convex constraint set for λ_{CH} is given by

$$\mathcal{C}_{\mathrm{CH}} = \{\mathbf{v} \in \mathbb{C}^2 : \mathrm{Im}(\mathbf{v}) \leq \mathbf{0}\} \ ,$$

where the imaginary part and inequality are interpreted component-wise. The projection operator for this set is simple to compute:

$$\mathrm{proj}_{\mathcal{C}_{\mathrm{CH}}}(\mathbf{y}) = \mathrm{Re}(\mathbf{y}) + \imath \min(\mathrm{Im}(\mathbf{y}), \mathbf{0}) \ ,$$

where, likewise, the minimum and real part operators are interpreted component-wise. The convex constraint set for λ_{ABV} is given by

$$\mathcal{C}_{\mathrm{ABV}} = \{\mathbf{v} \in \mathbb{R}^2 : \mathbf{v} \geq \mathbf{0}\} \ .$$

The projection operator for this set is also simple to compute:

$$\mathrm{proj}_{\mathcal{C}_{\mathrm{ABV}}}(\mathbf{y}) = \max(\mathbf{y}, \mathbf{0}) \ .$$

Finally, the convex constraint set for λ_{FS} is $\mathcal{C}_{\mathrm{FS}} = \mathbb{C}^{2N_c(\omega)+1}$ for which the projection operator is the identity map.

We use a similar strategy to the step length filtering strategy for the domain to select the step length. For example, in the λ_{ABV} model the updated parameters would be

$$\mathrm{proj}_{\mathcal{C}_{\mathrm{ABV}}}\left(\boldsymbol{\beta} - d\nabla_{\beta} F_{\lambda_{\mathrm{ABV}}}(\boldsymbol{\beta})/\eta_{\mathrm{filt}}^{n_{\mathrm{filt}}}\right) \ ,$$

where d is the original step length determined by the Cauchy point formula (23) and n_{filt} is the smallest ℓ with $0 \leq \ell \leq N_{\mathrm{filt}}$ such that

$$F_{\lambda_{\mathrm{ABV}}}\left(\mathrm{proj}_{\mathcal{C}_{\mathrm{ABV}}}\left(\boldsymbol{\beta} - d\nabla_{\beta} F_{\lambda_{\mathrm{ABV}}}(\boldsymbol{\beta})/\eta_{\mathrm{filt}}^{\ell}\right)\right) \leq F_{\lambda_{\mathrm{ABV}}}(\boldsymbol{\beta}) \ ,$$

with the convention that the step is size 0 if there is no ℓ satisfying the conditions. See algorithm 4 for pseudo-code of this procedure.

Remark 7. *While we did not use a Gauss-Newton descent direction for the impedance function optimization in the examples below, it can be done and there is one interesting phenomenon to note. If the curvature of the domain is nearly constant, say for a circular domain, the Jacobian matrix for the curvature dependent models is highly ill-conditioned. We found that one remedy was to compute the condition number of the Jacobian and revert to a constant impedance model if the condition number was above some threshold.*

Algorithm 4 $\ell^{\text{out}} = \text{OPTIMIZE\_IMPEDANCE}(\boldsymbol{\gamma},\, \ell,\, \omega,\, N_{\text{filt}},\, \eta_{\text{filt}})$

Minimize the residual with respect to the parameters of the impedance model for the impedance function, ℓ, holding the domain parameterization, $\boldsymbol{\gamma}$, fixed.

Input: $\boldsymbol{\gamma}$, ℓ, ω, N_{filt}, η_{filt}.

Initialize $R_0 \leftarrow R_\omega(\boldsymbol{\gamma}, \ell)$, $R_{\text{out}} \leftarrow R_0$, $\ell^{\text{out}} \leftarrow \ell$
$\mathbf{v} \leftarrow$ parameters of impedance model for ℓ
$\mathbf{g} \leftarrow -d\nabla_{\mathbf{v}} F_\lambda(\mathbf{v})$ ▷ F_λ is one of $F_{\lambda_{\text{ABV}}}$, $F_{\lambda_{\text{CH}}}$, $F_{\lambda_{\text{FS}}}$; see (23) for d
for $p = 1, \ldots, N_{\text{filt}}$ **do** ▷ Step-length filtering with projection
  $\mathbf{v}^S \leftarrow \text{proj}_{\mathcal{C}}(\mathbf{w} + \mathbf{g}/\eta_{\text{filt}}^p)$ ▷ $\mathcal{C}$ is one of $\mathcal{C}_{\text{ABV}}$, $\mathcal{C}_{\text{CH}}$, $\mathcal{C}_{\text{FS}}$
  if $R_\omega(\boldsymbol{\gamma}, \ell[\mathbf{v}^S]) < R_0$ **then**
    Update $\ell^{\text{out}} \leftarrow \ell[\mathbf{v}^s]$
    break

Output: ℓ^{out}.

Algorithm 5 $\hat{\boldsymbol{\gamma}}, \hat{\ell} = \text{ALTERNATING\_MIN}(\boldsymbol{\gamma}_0,\, \ell_0, \omega,\, N_f, N_{\text{inner}}, N_{\text{filt}}, \sigma_{\text{filt}}, \eta_{\text{filt}},\, \epsilon_R,\, \epsilon_{s,\Gamma},\, \epsilon_{s,\lambda},\, \epsilon_{s,R})$

Alternating between minimizing the residual as a function of the domain and impedance parameters. Check for convergence and stalling.

▷ $\boldsymbol{\gamma}$ and ℓ are parameterizations of the domain and impedance, respectively.

Input: $\boldsymbol{\gamma}_0$, ℓ_0, ω, N_f, N_{inner}, N_{filt}, σ_{filt}, η_{filt}, ϵ_R, $\epsilon_{s,\Gamma}$, $\epsilon_{s,\lambda}$, $\epsilon_{s,R}$

$N_{\text{samp}} \leftarrow 2N(\omega) + 1$
$\mathbf{w}_0 \leftarrow \text{FOURIER\_SERIES\_COEFFICIENTS}(\boldsymbol{\gamma}_0,\, \{j/N_{\text{samp}}\}_{j=1}^{N_{\text{samp}}}, N(\omega))$
$\mathbf{v}_0 \leftarrow$ impedance function parameters of ℓ_0
$R_0 \leftarrow R_\omega(\boldsymbol{\gamma}_0, \ell_0)$
for $q = 1, \ldots, N_f$ **do**
  $\boldsymbol{\gamma}_q, \ell_q \leftarrow \text{OPTIMIZE\_DOMAIN}(\boldsymbol{\gamma}_{q-1},\, \ell_{q-1},\, \omega,\, N_{\text{filt}},\, \sigma_{\text{filt}},\, \eta_{\text{filt}})$
  for $p = 1, \ldots, N_{\text{inner}}$ **do**
    $\ell_q \leftarrow \text{OPTIMIZE\_IMPEDANCE}(\boldsymbol{\gamma}_q,\, \ell_q,\, \omega,\, N_{\text{filt}},\, \eta_{\text{filt}})$
  $\hat{\boldsymbol{\gamma}},\, \hat{\ell} \leftarrow \boldsymbol{\gamma}_q,\, \ell_q$
  $R_q \leftarrow R_\omega(\boldsymbol{\gamma}_q, \ell_q)$
  if $R_q < \epsilon_R$ **then** ▷ Check for convergence
    break
  $\mathbf{w}_q \leftarrow \text{FOURIER\_SERIES\_COEFFICIENTS}(\boldsymbol{\gamma}_q,\, \{j/N_{\text{samp}}\}_{j=1}^{N_{\text{samp}}}, N(\omega))$
  $\mathbf{v}_q \leftarrow$ impedance function parameters of ℓ_q
  if $\|\mathbf{w}_q - \mathbf{w}_{q-1}\| \le \epsilon_{s,\Gamma}\|\mathbf{w}_q\|$ **then** ▷ Check for stagnation
    break
  if $\|\mathbf{v}_q - \mathbf{v}_{q-1}\| \le \epsilon_{s,\lambda}\|\mathbf{v}_q\|$ **then**
    break
  if $|R_q - R_{q-1}| \le \epsilon_{s,R} R_q$ **then**
    break

Output: $\hat{\boldsymbol{\gamma}}$, $\hat{\ell}$

4 Numerical results

The numerical experiments in this section explore the suitability of impedance models for dissipative transmission problems. We describe common test settings here. Tests with data generated by an impedance model are in Section 4.1 and tests with data generated by a transmission model are in Sections 4.2 and 4.3.

Reproducibility The scripts used to generate these results [8] and the data associated with the figures [6] are publicly available and archived.

Test data parameters Each test has a range of pulsation frequencies, which are determined by the value $k_2^{\max}$, taken to be an integer. In particular, the values of ω are of the form

$$\omega_j = c_2\,(1 + (j-1)/2)$$

where $j = 1, \ldots, 2k_2^{\max}+1$. Thus, there are $N_k = 2k_2^{\max}+1$ frequencies and the exterior wave speeds range from 1 to $k_2^{\max}$, with a spacing of $1/2$. The value of $k_2^{\max}$ is selected so that the obstacle can be reasonably well reconstructed from data at the highest frequency.

For most of the examples, we assume best-case data in the sense that there are sufficiently many incident directions and receptor locations to obtain a good reconstruction and that the data are full aperture. In particular, unless otherwise noted, the data are collected at all receptors for each incident angle, the number of incident directions and receptors is set to $N_d(\omega) = N_r(\omega) = \lfloor 10\omega/c_2 \rfloor$, the incident directions are set to $\mathbf{d}_i = (\cos(\theta_i), \sin(\theta_i))$ for $i = 1, \ldots, N_d(\omega)$ with $\theta_i = 2\pi i/N_d(\omega)$, and the receptors are located at the points $\mathbf{r}_i = (r\cos(\theta_i), r\sin(\theta_i))$ for $i = 1, \ldots, N_r(\omega)$ with $r = 10$.

One of our primary interests below is the performance of the model as the dissipation, δ, varies. As a reference dissipation value, we use $\delta_0 = \sqrt{3}k_2^{\max}$, which is suggested in [4] as a value of dissipation where the asymptotic model should become accurate for the highest pulsation in the data. The remaining physical parameters are fixed as $c_1 = 0.5$, $c_2 = 1.0$, $\rho_1 = 1.2$, and $\rho_2 = 0.7$, so that $c_r = 0.5$ and $\rho_r \approx 1.7$. This corresponds to the obstacle having a denser material and a higher acoustic wave speed. We found that the results were similar if instead $c_r > 1$ and $\rho_r < 1$, though we did not explore the extremes.

Measures of error When applying continuation-in-frequency, we obtain a sequence of approximations of the domain, $\{\hat{\Gamma}_j\}_{j=1}^{N_k}$, and impedance functions, $\{\hat{\lambda}_j\}_{j=1}^{N_k}$, corresponding to the solution obtained at the frequencies $\{\omega_j\}_{j=1}^{N_k}$. We consider two quantitative error measurements for a given reconstruction of the domain and impedance function $\hat{\Gamma}, \hat{\lambda}$. The first is the relative residual at a given frequency; see (22). Below, we always plot $R_{\omega_j}(\hat{\Gamma}_j, \hat{\lambda}_j)$. The second error measurement is the relative area of the symmetric difference between the interior of the true obstacle, $\Omega_\star$, and the interior of the recovered obstacle, $\hat{\Omega}$ (which has boundary $\hat{\Gamma}$):

$$E(\hat{\Gamma}) = \frac{\text{area}(\Omega_\star \setminus \hat{\Omega}) + \text{area}(\hat{\Omega} \setminus \Omega_\star)}{\text{area}(\Omega_\star)} \,. \tag{25}$$

We approximate the areas in (25) based on the polygons defined by the boundary nodes of $\Omega_\star$ and $\hat{\Omega}$. This is an inherently low order approximation but appears to provide at least 2 digits of precision in the examples below.

Discretization, regularization, and optimization method parameters The PDEs are discretized using high order boundary integral equation methods as described in Appendix A. We discretize the boundary curve using approximately 10 points per wavelength by setting $N(\omega) = \max(\lceil 5\omega L/(c_2\pi)\rceil, 300)$, where L is the length of the current approximation of the domain. This ensures that the forward map, $\mathcal{F}^{\text{imp}}$, and its Fréchet derivatives are evaluated accurately.

Unless otherwise noted, the initial guess for the geometry, $\hat{\Gamma}_0$ is a unit circle centered at the origin. The initial guess for the impedance function is always $\hat{\lambda}_0 \equiv 1$.

In most of the examples, the data are generated using the forward model with transmission boundary conditions and the inverse problem is solved using the model with impedance boundary conditions, so that "inverse crimes" are avoided. However, this is not the case in Section 4.1. An inverse crime is still avoided there in that the data are generated using approximately 20 points per wavelength whereas the inverse problem uses 10, the non-airplane domains are not originally parameterized in arc-length whereas the inverse solver constantly resamples in arc-length, and the true boundary curve is generally not contained in the constraint set at the lowest frequencies. We have also added random noise to this data on the order of 10 times the (approximate) discretization error.

The search direction for the domain boundary update, h, is regularized by limiting the length of its real Fourier series. This length is $2N_\gamma(\omega) + 1$ and $N_\gamma(\omega)$ should be proportional to ω so that h does not contain features smaller than half of a wavelength. We set $N_\gamma(\omega) = \lfloor \omega L/(c_2\pi)\rfloor$, where L is the length of the current approximation of the domain. The λ_{FS} model is also regularized by limiting the length of its Fourier series. This length is $2N_c(\omega) + 1$ and we set $N_c(\omega) = N_\gamma(\omega)/2$ following the advice of [21]. The constraint set $S_\Gamma(\omega)$ is determined by the amount of curvature regularization used. The idea is that the amount of elastic energy contained in the first $M(\omega)$ modes of the curvature should exceed some proportion of the total elastic energy, i.e. $\sqrt{\mathcal{E}^{M(\omega)}} \geq C_H\sqrt{\mathcal{E}(\Gamma)}$; cf. (7). We set $C_H = 0.9$ and $M(\omega) = N_\gamma(\omega)$. While reasonable criteria for setting N_γ and N_c are understood, it is less clear how to select C_H and the solution of the inverse problem appears to be mildly sensitive to this parameter. The value of $C_H = 0.9$ was found to work on nearly all of the examples; see Section 4.3 for an exception.

For detailed descriptions of the optimization parameters, refer to Section 3. Alternating minimization is performed with a maximum of $N_f = 40$ iterations and $N_{\text{inner}} = 5$ inner iterations for the impedance solver, with tolerance $\epsilon_R =$

10^{-4} and stagnation parameters $\epsilon_{s,\Gamma} = \epsilon_{s,\lambda} = \epsilon_{s,R} = 10^{-4}$. The values of N_f, ϵ_R, and the stagnation parameters are quite conservative; the tolerance is never reached in the examples with transmission data below and stagnation could likely be detected earlier without much effect on the quality of the solution. We set a maximum of $N_{\text{filt}} = 3$ filtrations per step. Step length filtering is performed with $\eta_{\text{filt}} = 8$ and Gaussian filtering is performed with $\sigma_{\text{filt}} = 10^{-1}$. These filtering parameters are aggressive so that the limited number of filtration steps can be effective, with the overall goal of reducing the number of PDEs that must be solved during filtering.

4.1 Experiments with impedance data

Here we compare the performance of the three impedance models, λ_{FS}, λ_{CH}, and λ_{ABV}, for impedance data generated by the model of [5], i.e. generated as the solution of (2) with the impedance model (3) and the dissipation set as $\delta = \delta_0 = \sqrt{3}k_2^{\max}$. We consider 4 different obstacle shapes. In Figure 2, the first corresponds to a smooth obstacle shape parameterized as $(r(t)\cos(t), r(t)\sin(t))$ with $r(t)$ given as constant perturbed by a random Fourier series ($k_2^{\max} = 20$), the second row is a smooth airplane-like obstacle ($k_2^{\max} = 30$), the third row is a more detailed airplane-like obstacle ($k_2^{\max} = 40$), and the fourth row is a smooth starfish-like obstacle ($k_2^{\max} = 30$).

Specifically, the random obstacle has

$$r(t) = a_0 + \sum_{j=1}^{7} a_j \cos(2\pi j t) + b_j \sin(2\pi j t) \ ,$$

where $\mathbf{a} = (1, , 0.0540, -0.0217, 0.1189, 0.1317, -0.0406, -0.0445, 0.1328)$ and $\mathbf{b} = (0.0834, 0.0604, -0.0107, 0.0003, 0.0457, 0.0922, -0.0197)$. The starfish obstacle is of the same form, except that most of the a_j and b_j are zero except for $a_0 = 1$ and $a_5 = 0.3$. The airplane obstacles are obtained from an image of the silhouette of an airplane (see file "SU571.png" in the repository [8]). To obtain a smooth parameterization of the shape of the plane, we first obtain an initial set of boundary points (function `bwboundaries` in MATLAB). There are 2029 points returned by this function. We then resample a Fourier interpolant of these points to obtain N_{pts} roughly equispaced points on its boundary. Then, we approximate the two periodic functions defined by the x coordinates and y coordinates of the N_{pts} boundary points by a periodic cubic spline interpolant. For the less detailed smooth airplane-like obstacle, we use $N_{\text{pts}} = 20$ and for the detailed airplane-like obstacle, we use $N_{\text{pts}} = 70$. This operation is available in the file "smooth_plane.m" of the repository [8].

The three models perform equally well on the first three obstacles. To the eye, these are capable of recovering sharp features and non-convex features of the more detailed airplane. The λ_{ABV} model appears to have a slight edge over the λ_{CH} model, which can be seen most clearly by comparing the results obtained for the two at pulsation $\omega = 10$.

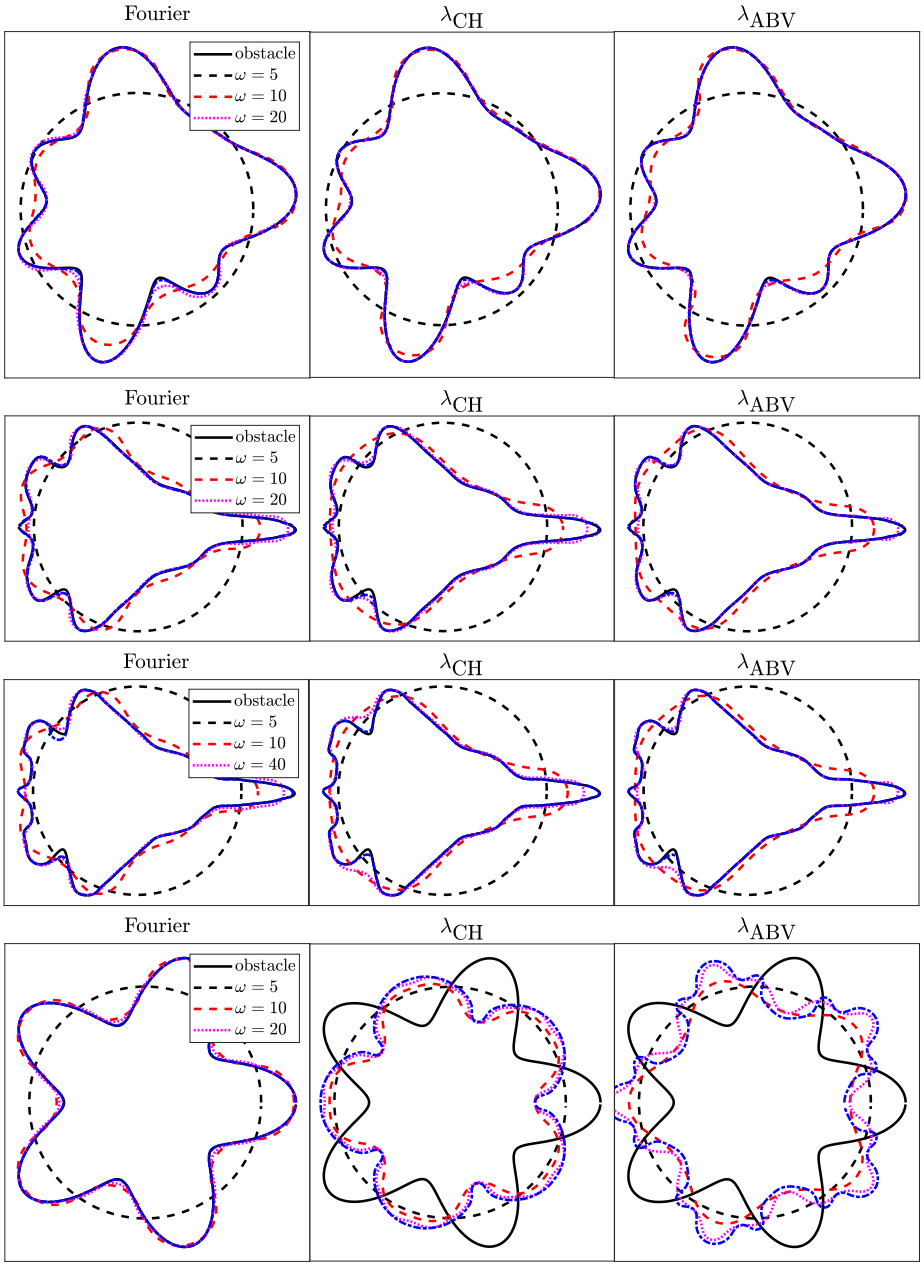

Figure 2: Reconstructions of the domains obtained for the experiments with impedance data of Section 4.1. The top row corresponds to a "random" obstacle, the second row a smooth "airplane" obstacle, the third row a more detailed "airplane" obstacle, and the bottom row a "starfish" obstacle. Each column is labeled by the impedance model used in the inverse problem.

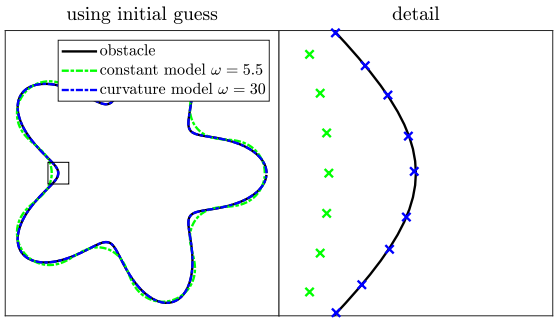

Figure 3: Using a different initializer for the starfish domain in the impedance data experiment of Section 4.1. Here we show an initial guess obtained from solving the inverse problem with a constant impedance model up to frequency $\omega = 5.5$ and the refined inverse problem solution obtained by the λ_{ABV} model starting with this initial guess at the next frequency ($\omega = 6$).

The constrained, curvature-dependent models fail on the starfish-like obstacle. These models get caught in a local minimum that has the same symmetry as the domain. Based on the results of the random smooth domain, which is similarly constructed, and the airplane domains, which have reflective symmetry, it appears that this phenomenon is specific to this type of starfish-like domain in which the distance from the origin is correlated with the curvature of the domain. The λ_{FS} model avoids this issue because we select $N_c(\omega)$ to be $N_\gamma(\omega)/2$, which forces the optimization problem to resolve the domain first. In contrast, the curvature-dependent models can have Fourier content that is similar to the obstacle.

While this failure mode is worthy of note, we believe it to be unlikely to appear in applications. It can also be mitigated by first solving the inverse problem with a constant impedance model up to a certain frequency and then switching to the curvature-dependent model; see Figure 3 for an example of this.

The above results show that the λ_{ABV} and λ_{CH} models can perform as well as the more general model λ_{FS}, at least when the data are generated by a boundary condition in the class covered by these models. This impedance boundary condition is interesting because it is an approximation of the transmission boundary condition for dissipative media. Because λ_{ABV} is specifically designed for this kind of data and it is straightforward to reconstruct the material parameters from λ_{ABV}, we will focus on its performance on transmission data in the sections below. We again compare λ_{ABV} to alternative models for the transmission problem in Section 4.2.4, including λ_{FS}, where λ_{ABV} is observed to offer some advantages.

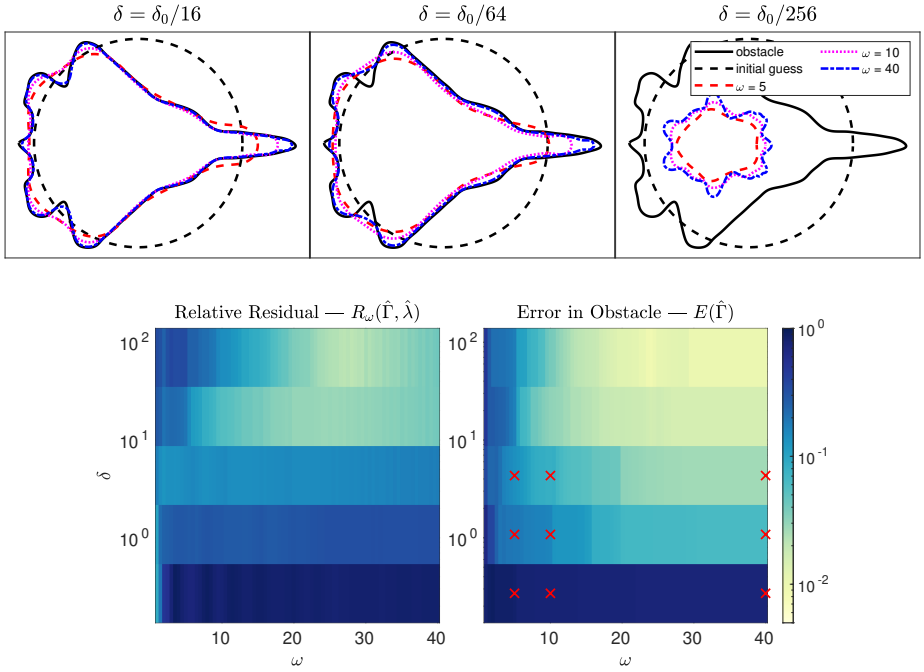

Figure 4: Experiment of Section 4.2.1 with transmission data using the λ_{ABV} impedance model for the inverse problem. The top row shows reconstructions obtained for different values of the pulsation, ω, and dissipation, δ. The bottom row has plots of the error measures as a function of ω and δ. The values of (ω, δ) for the reconstructions in the top row are marked in red in the error plot.

4.2 Experiments with transmission data

The results of this section are for data generated by the transmission problem, (1), for the more detailed airplane-like obstacle. In all examples in this section, $k_2^{\max} = 40$. The model used for the inverse problems is always the impedance model, (2), with the λ_{ABV} model for the impedance function, unless otherwise noted.

4.2.1 Effect of lowering dissipation

The λ_{ABV} model is known to be more accurate for higher levels of dissipation, with $\delta_0 = \sqrt{3}k_2^{\max}$ providing good quantitative agreement in the scattered data of the impedance and transmission models [4].

In this experiment, we generate transmission scattering data for the more detailed airplane with $\delta = \delta_0/4^j$ for $j = 0, 1, 2, 3, 4$. We then solve the inverse problem with the λ_{ABV} model for each data set. The results are shown in Figure 4.

We find that a reasonably close reconstruction of the obstacle is obtained

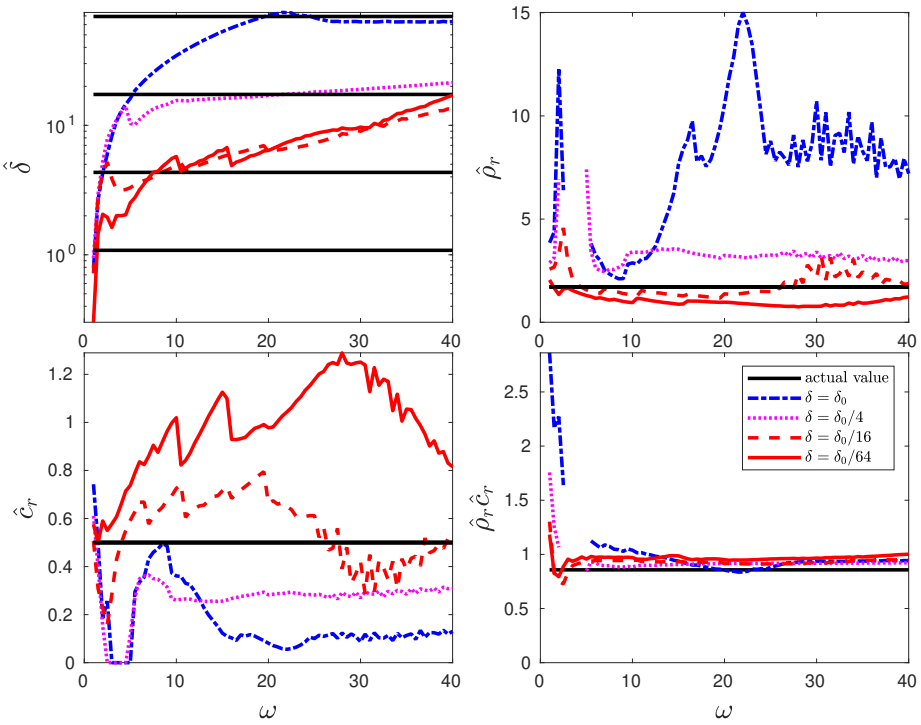

Figure 5: Experiment of Section 4.2.1 with transmission data using the λ_{ABV} impedance model for the inverse problem. Each plot shows the recovery of a physical parameter for various values of the dissipation, δ, as a function of the pulsation, ω.

for dissipation as low as $\delta = \delta_0/64$. For $\delta = \delta_0/256$, the reconstruction fails completely.

Given the parameters $\hat{\boldsymbol{\beta}}$ recovered by solving the inverse problem with the λ_{ABV} model, we can recover approximations of the physical parameters, denoted $\hat{\rho}_r$, $\hat{c}_r$, $\hat{\delta}$, from the relations (14). Figure 5 plots $\hat{\delta}$, $\hat{\rho}_r$, $\hat{c}_r$ and $\hat{\rho}_r\hat{c}_r$ as a function of the pulsation for various values of the dissipation, δ. Because the obstacle recovery improves as ω increases, it is expected that the recovered parameters should be better for higher values of the pulsation. The value of $\hat{\delta}$ is reasonably accurate for higher levels of dissipation, but it gives an overestimate for lower levels of dissipation. In most cases, the recovered values $\hat{\rho}_r$ and $\hat{c}_r$ are not particularly accurate. However, the product $\hat{\rho}_r\hat{c}_r$ is relatively accurate in most regimes. We suspect that this is because the product $\hat{\rho}_r\hat{c}_r$ appears in the constant term of the λ_{ABV} model, whereas only $\hat{\rho}_r$ appears in the curvature term; cf. (3).

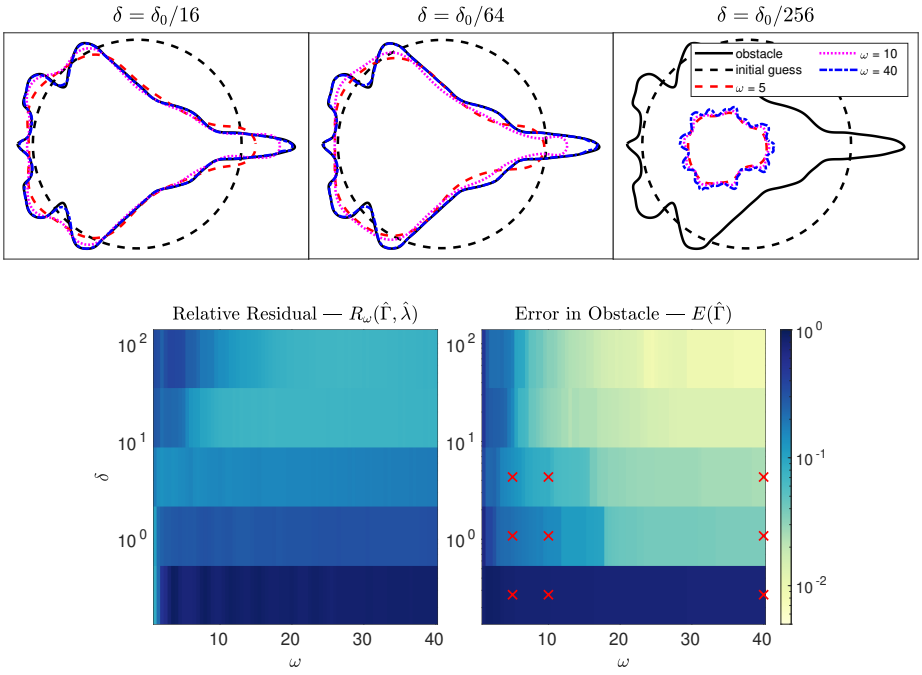

Figure 6: Experiment of Section 4.2.2 with noise-corrupted transmission data using the λ_{ABV} impedance model for the inverse problem. The top row shows reconstructions obtained for different values of the pulsation, ω, and dissipation, δ. The bottom row has plots of the error measures as a function of ω and δ. The values of (ω, δ) for the reconstructions in the top row are marked in red in the error plot.

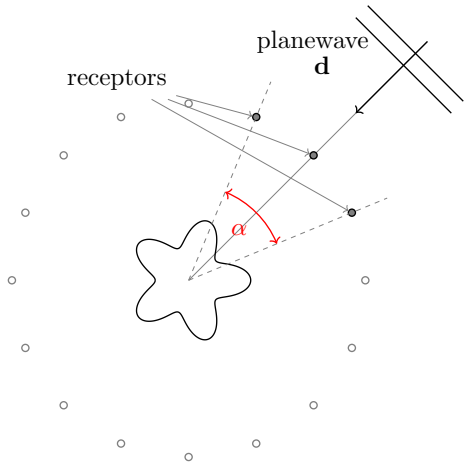

Figure 7: Illustration of arrangement of receptors for backscatter data.

4.2.2 Experiment with noise

Here we explore the effect of additive noise on the recovery of the airplane. We assume that the measured values are now of the form

$$\mathbf{u}^{\text{meas}}_{\omega,\mathbf{d}} = \mathcal{F}^{\text{trans}}_{\omega,\mathbf{d}}(\Gamma_\star) + \Sigma(\omega)\boldsymbol{\eta}\,, \tag{26}$$

where the entries of $\boldsymbol{\eta} \in \mathbb{C}^{N_r}$ are drawn from the standard normal distribution and $\Sigma(\omega) = \sigma \max_{\mathbf{d}} |\mathcal{F}^{\text{trans}}_{\omega,\mathbf{d}}(\Gamma_\star)|$ for some constant σ.

In this experiment, we generate transmission scattering data for the more detailed airplane with $\delta = \delta_0/4^j$ for $j = 0, 1, 2, 3, 4$. We then solve the inverse problem with the λ_{ABV} model for each data set and $\sigma = 10^{-1}$. The results are shown in Figure 6.

The effect of the noise is visible in the residual plot, where the smallest values of the residual are similar to σ and about an order of magnitude larger than in the noise-free case (cf. Figure 4). On the other hand, the actual recovered domain performs at least as well (and in some cases better) than in the noise-free case. This suggests that the recovery is reasonably robust to additive noise.

4.2.3 Experiment with backscatter data

In the examples above, we have best-case scattering data, in that the receptors surround the obstacle, there are many incident directions, and the data are available at all receptors for each incident wave. Such data may not be available in all applications. Here we consider the recovery problem for backscatter data. The backscatter set-up is illustrated in Figure 7. For this problem, we have the same set of possible receptor locations as for the experiments above, but for each incident wave we assume that measurements are only available within a certain angle (α in the figure) about the axis defined by the planewave direction. For

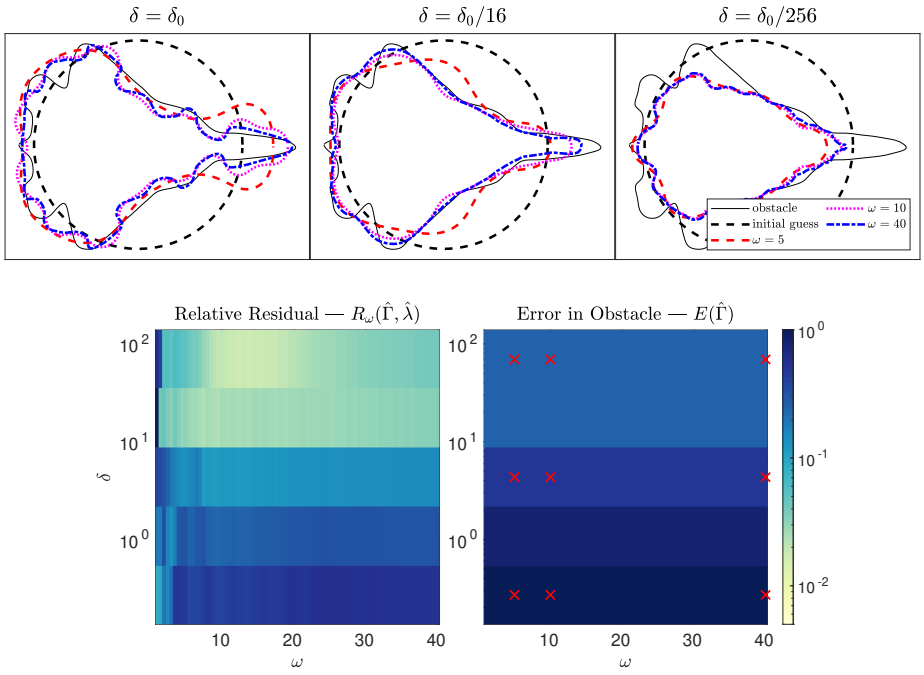

Figure 8: Experiment of Section 4.2.3 with backscatter transmission data using the λ_{ABV} impedance model for the inverse problem. The top row shows reconstructions obtained for different values of the pulsation, ω, and dissipation, δ. The bottom row has plots of the error measures as a function of ω and δ. The values of (ω, δ) for the reconstructions in the top row are marked in red in the error plot.

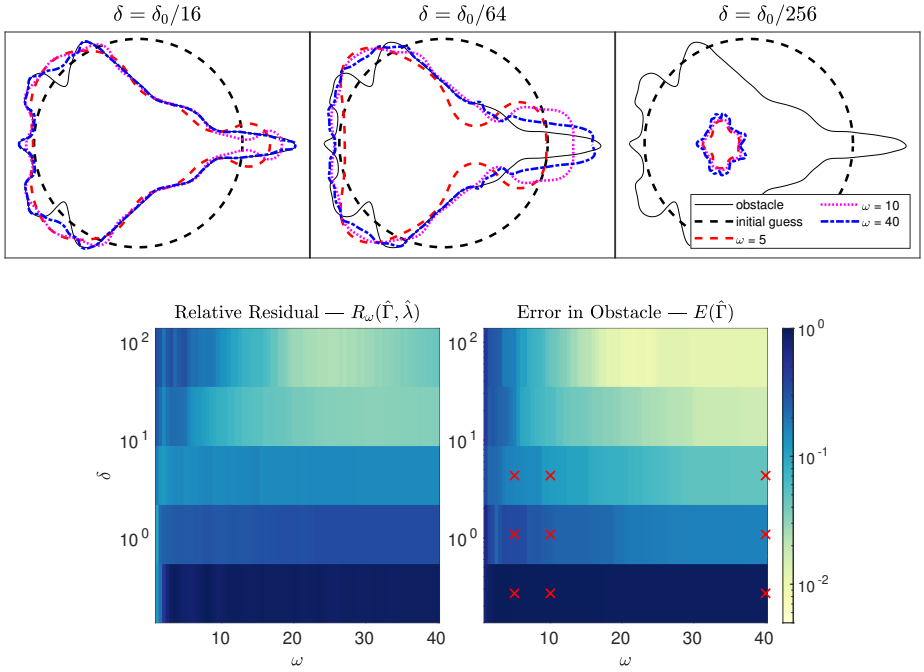

Figure 9: Experiment of Section 4.2.4 with transmission data using the λ_{FS} impedance model for the inverse problem. The top row shows reconstructions obtained for different values of the pulsation, ω, and dissipation, δ. The bottom row has plots of the error measures as a function of ω and δ. The values of (ω, δ) for the reconstructions in the top row are marked in red in the error plot.

the experimental results here, $\alpha = \pi/4$, so that the data set is 1/8th the size of the data set in Section 4.2.1.

The results for backscatter data are shown in Figure 8. The residual plot has minima at the lowest frequencies, where the optimization procedure appears to get caught in local minima. While the recovered domains bear some visual resemblance to the true domain, the recovery is not particularly accurate for any value of dissipation.

4.2.4 Experiments with alternative models

In these experiments, we verify that the curvature-dependent model provides a meaningful advantage over other models in certain regimes.

General Fourier series model At sufficiently high frequencies, the λ_{FS} model should be able to approximate the λ_{ABV} model and thus the resulting residuals should be just as good. We provide the recovery results for the λ_{FS} model applied to the same data as the experiment of Section 4.2.1 in Figure 9.

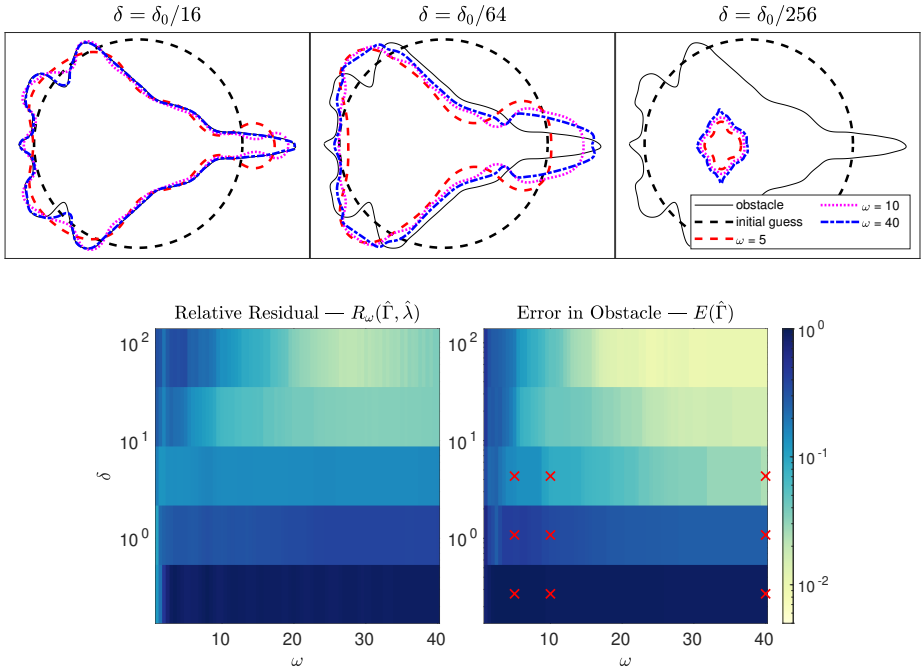

Figure 10: Experiment of Section 4.2.4 with transmission data using a constant impedance model for the inverse problem. The top row shows reconstructions obtained for different values of the pulsation, ω, and dissipation, δ. The bottom row has plots of the error measures as a function of ω and δ. The values of (ω, δ) for the reconstructions in the top row are marked in red in the error plot.

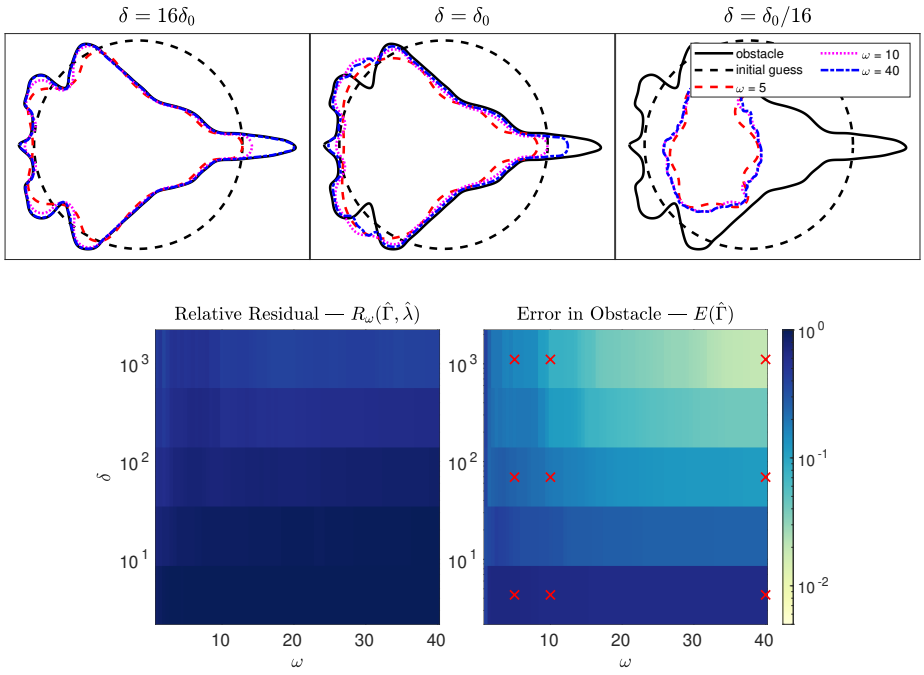

Figure 11: Experiment of Section 4.2.4 with transmission data using a sound-hard model for the inverse problem. The top row shows reconstructions obtained for different values of the pulsation, ω, and dissipation, δ. The bottom row has plots of the error measures as a function of ω and δ. Note that the range of δ values is different from the other examples. The values of (ω, δ) for the reconstructions in the top row are marked in red in the error plot.

For high levels of dissipation, the λ_{FS} model works as well as λ_{ABV} in terms of both the reconstruction error and the residual. However, for lower levels of dissipation, particularly $\delta_0/16$ and $\delta_0/64$, the λ_{ABV} model obtains a visually good reconstruction while the λ_{FS} model does not. Thus, the more constrained λ_{ABV} model appears to provide more robust shape recovery in this regime.

Constant impedance model Above, the failure mode of the curvature-dependent impedance models was addressed by first seeking a minimum with the constant impedance model and then using the obtained domain as an initial guess. To explore the viability of this simpler model in general, we provide the recovery results for the constant impedance model applied to the same data as the experiment of Section 4.2.1 in Figure 10. The results are similar to the results obtained by the more general λ_{FS} model so that the constant impedance model is a compelling alternative to λ_{FS}, though not as performant as λ_{ABV} for lower dissipation.

Neumann boundary condition model As δ increases, we have that $\lambda_{\mathrm{ABV}} = \mathcal{O}(\delta^{-1/2})$. In the limit, we then expect that the obstacle would behave as a sound-hard obstacle. Here, we will test how well the sound-hard model does for the recovery of the obstacle in the dissipative setting.

Let $\mathcal{F}^{\mathrm{neu}}_{\omega,\mathbf{d}}(\Gamma)$ be the vector of values of $\phi(\mathbf{r}_j)$ where ϕ is the solution of the PDE

$$\begin{aligned} -(\Delta + k_2^2)\phi &= 0 && \text{in } \Omega_2 \ , \\ \partial_n \phi &= -\partial_n u^{\mathrm{inc}} && \text{on } \Gamma \ , \\ \sqrt{|\mathbf{x}|}\left(\phi - ik_2 \frac{\mathbf{x}}{|\mathbf{x}|}\cdot\nabla\phi\right) &\to 0 && \text{as } |\mathbf{x}| \to \infty \ . \end{aligned} \tag{27}$$

We will solve the minimization problem

$$\hat{\Gamma}_j = \underset{\Gamma \in S_\Gamma(\omega_j)}{\arg\min} \sum_{i=1}^{N_d} |\mathbf{u}^{\mathrm{meas}}_{\omega_j,\mathbf{d}_i} - \mathcal{F}^{\mathrm{neu}}_{\omega_j,\mathbf{d}_i}(\Gamma)|^2 \ , \tag{28}$$

using similar tools to the ones we applied to the impedance model. We consider a different range of values for the dissipation; we set $\delta = \delta_0/4^j$ for $j = -2, -1, 0, 1, 2$.

The recovery results are shown in Figure 11. While the Neumann model can recover the domain for the largest values of the dissipation, the recovery obtained for $\delta \leq \delta_0$ has significant error.

4.3 A domain with corners

In these experiments, we explore the behavior of the recovery process for a domain with corners. The true domain is an "L"-shaped domain with the vertices $\{(0,0),(2,0),(2,1),(1,1),(1,2),(0,2)\}$. The solution of the scattering problem

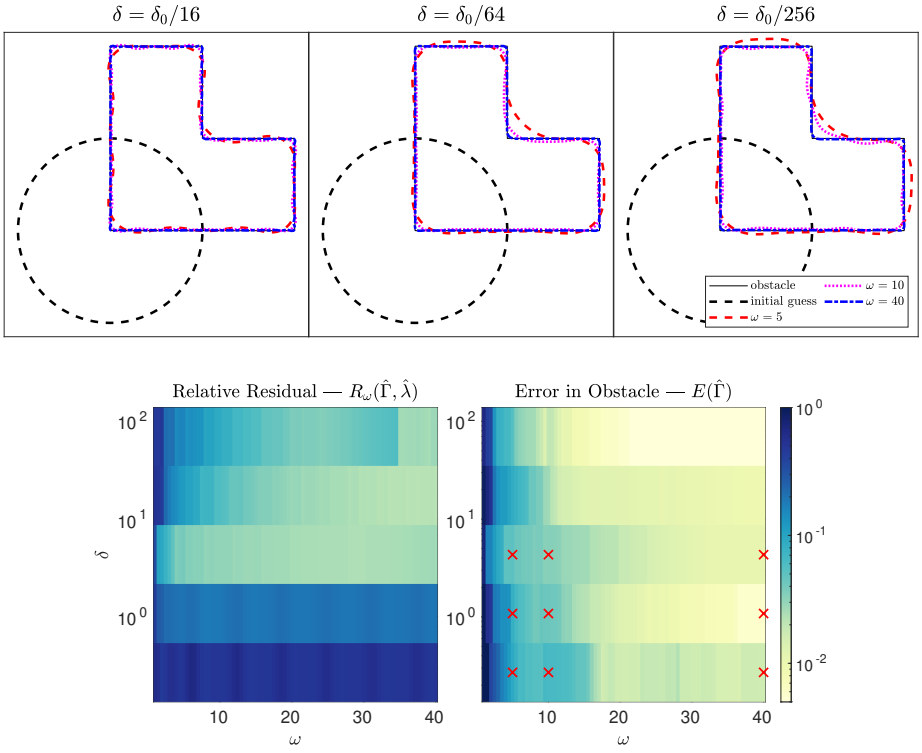

Figure 12: Experiment of Section 4.3 with transmission data generated by an "L"-shaped domain, using the λ_{ABV} impedance model for the inverse problem. The top row shows reconstructions obtained for different values of the pulsation, ω, and dissipation, δ. The bottom row has plots of the error measures as a function of ω and δ. The values of (ω, δ) for the reconstructions in the top row are marked in red in the error plot.

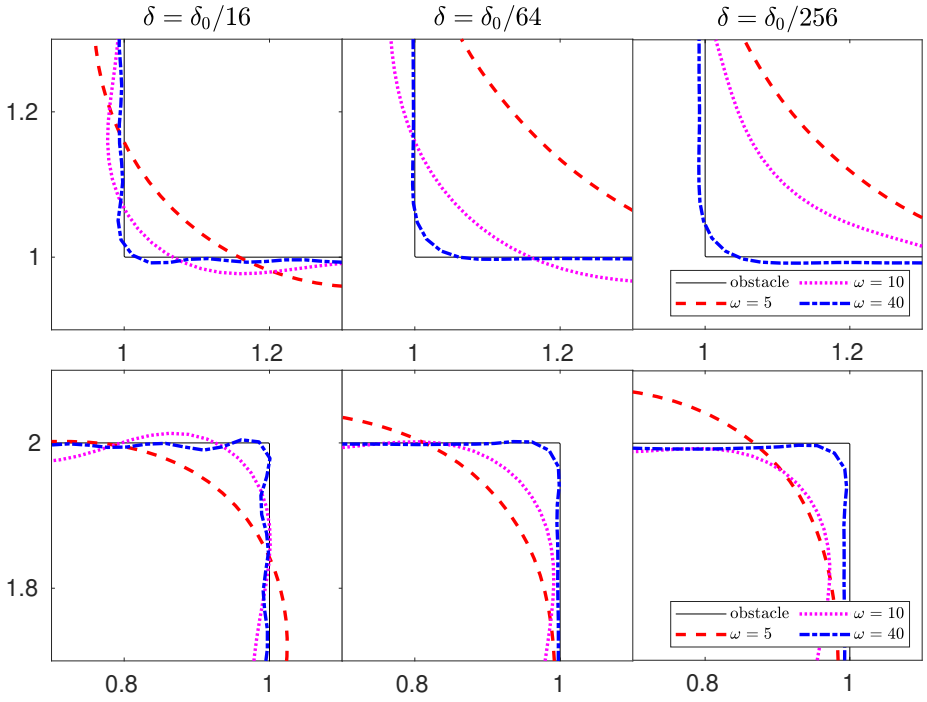

Figure 13: Detail of reconstructions near corners for the experiment of Section 4.3 with transmission data generated by an "L"-shaped domain, using the λ_{ABV} impedance model for the inverse problem. The top row corresponds to the re-entrant corner at $(1, 1)$ and the bottom row corresponds to the corner at $(1, 2)$.

on this domain requires different solvers than the the previous examples because the associated boundary integral equation will have solutions with singularities near the corners; see Appendix A.3 for details. As in most examples above, we generate scattering data for varying levels of dissipation, $\delta = \delta_0/4^j$ for $j = 0, 1, 2, 3, 4$ and make full aperture measurements.

In contrast with the experiments above, the solution of the inverse problem with the λ_{ABV} model for this data appears to be more sensitive to the selection of C_H, which determines the amount of curvature regularization. To deal with this, we solve the inverse problem with $C_H = 0.9$ and $C_H = 0.95$ and then keep the solution with smaller residual at the highest frequency for the results in Figure 12. In particular, the $\delta = \delta_0$ reconstruction is better with $C_H = 0.9$ and the $\delta = \delta_0/4$ reconstruction is better with $C_H = 0.95$ (in both cases the worse reconstruction is stuck in a local minimum), while the remaining δ values have similar performance for either value of C_H.

We find that a reasonably close reconstruction of the obstacle is obtained for dissipation as low as $\delta = \delta_0/256$, even though the relative residual indicates

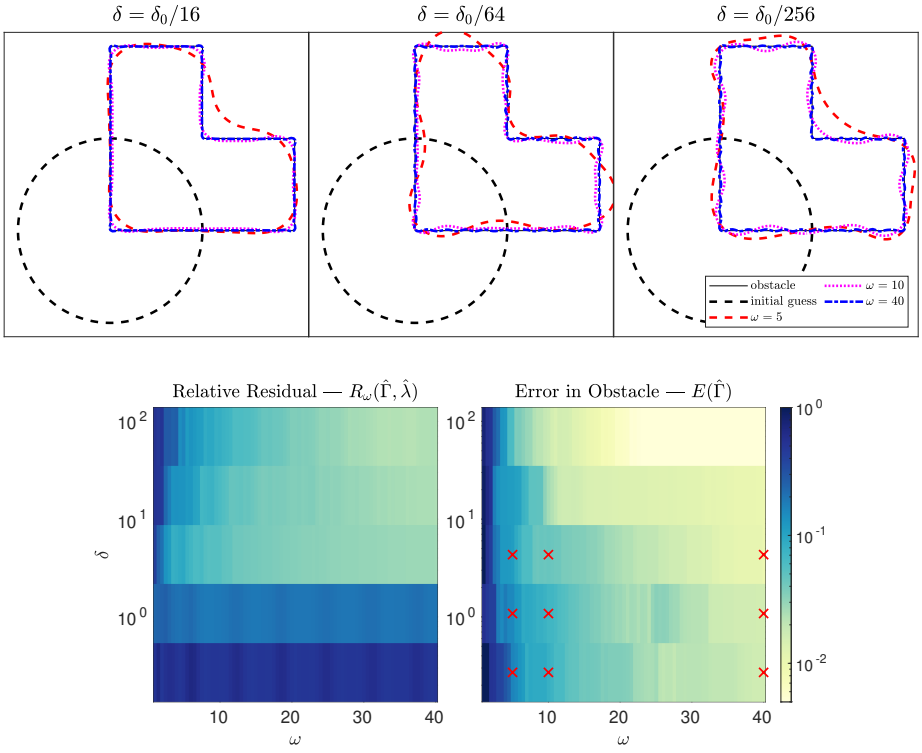

Figure 14: Experiment of Section 4.3 with transmission data generated by an "L"-shaped domain, using a constant impedance model for the inverse problem. The top row shows reconstructions obtained for different values of the pulsation, ω, and dissipation, δ. The bottom row has plots of the error measures as a function of ω and δ. The values of (ω, δ) for the reconstructions in the top row are marked in red in the error plot.

that the model is not particularly accurate for this level of dissipation. This is a little better than observed for the airplane. Notably, the "L"-shape does not have particularly narrow features, so that waves are not transmitting as significantly as they do for the plane.

In general, it appears that the model still works well for data generated by a domain with corners. We plot details of the reconstructions near the corners in Figure 13. The $\delta = \delta_0/16$ reconstruction shows mild oscillatory behavior near the corners, while the $\delta = \delta_0/256$ and $\delta = \delta_0/64$ reconstructions are smoother but not as near to the original curve. This is because the C_H value in the $\delta_0/16$ plot is $C_H = 0.9$, while it is $C_H = 0.95$ in the $\delta_0/64$ and $\delta_0/256$ plots. Thus, the latter plots were generated with more regularization.

We include results using a constant impedance model in Figure 14, using the same strategy of choosing the best performance out of two reconstructions obtained for $C_H = 0.9$ and $C_H = 0.95$. The model performs reasonably well, though the residuals and errors are larger than the λ_{ABV} model, particularly for lower levels of dissipation. Thus, the curvature-dependent model provides an advantage even for flat domains with corners. Intuitively, a smooth approximation of a corner will encode information about the angle of the corner in the sign and magnitude of its curvature near the corner.

5 Conclusion and future directions

We have developed an optimization framework for using curvature-dependent impedance models, like λ_{ABV}, to solve inverse problems with transmission data from a dissipative obstacle. The model succeeds in recovering the obstacle boundary reasonably accurately, even at values of the dissipation for which waves transmit through the narrowest parts of the obstacle. Intuitively, the model fails for lower amounts of dissipation where many waves transmit.

The recovered material parameters are relatively accurate for the dissipation, δ, and the product of the relative sound speed and relative density, $c_r\rho_r$, but the individual values of c_r and ρ_r appear more difficult to recover. Because the domain is recovered well with the impedance model, we plan to explore the use of a transmission model as a post-processing step to obtain more accurate material parameters once the domain is set.

The model appears to be robust to (and may benefit from) additive noise and provides a meaningful advantage over simpler models, like constant impedance or Neumann boundary conditions, in terms of the range of values of the dissipation to which it applies. Because an impedance model can emulate both Neumann and Dirichlet boundary conditions in certain limits [21], we believe that these results further support the use of a curvature-dependent impedance model as a first-pass model for any scattering data.

While the λ_{ABV} model was the focus of the numerical experiments, the similar λ_{CH} model is more general and achieves results nearly as good. We plan to explore the performance of λ_{CH} in more settings; for example, the more constrained λ_{ABV} is specific to the type of transmission boundary condition consid-

ered here but λ_{CH} could conceivably be used as a model for other transmission conditions and thin coatings.

Finally, the lackluster results with backscatter data suggest that further work is needed for certain experimental settings. Our experience is that manipulating the $M(\omega)$ and C_H parameters was insufficient to improve the situation. We plan to investigate improved regularization strategies and more sophisticated optimization methods in these regimes.

Acknowlegments

The authors would like to thank Jeremy Hoskins and Manas Rachh for many useful discussions.

Funding The work of C. Borges was supported in part by the Office of Naval Research under award number N00014-21-1-2389.

Data availability statement

The data that support the findings of this study are openly available. Specifically, the scripts used to generate these results [8] and the data associated with the figures [6] are publicly available.

References

[1] I. Akduman and R. Kress. Direct and inverse scattering problems for inhomogeneous impedance cylinders of arbitrary shape. *Radio Science*, 38(3), 2003. URL `https://doi.org/10.1029/2002RS002631`.

[2] B. K. Alpert. Hybrid gauss-trapezoidal quadrature rules. *SIAM Journal on Scientific Computing*, 20(5):1551–1584, 1999. URL `https://doi.org/10.1137/S1064827597325141`.

[3] X. Antoine and H. Barucq. Approximation by generalized impedance boundary conditions of a transmission problem in acoustic scattering. *ESAIM: Mathematical Modelling and Numerical Analysis*, 39(5):1041–1059, 2005. URL `https://doi.org/10.1051/m2an:2005037`.

[4] X. Antoine and H. Barucq. On the construction of approximate boundary conditions for solving the interior problem of the acoustic scattering transmission problem. In *Domain decomposition methods in science and engineering*, pages 133–140. Springer, 2005. URL `https://doi.org/10.1007/3-540-26825-1_9`.

[5] X. Antoine, H. Barucq, and L. Vernhet. High-frequency asymptotic analysis of a dissipative transmission problem resulting in generalized impedance boundary conditions. *Asymptotic Analysis*, 26(3-4):257–283, 2001.

[6] T. Askham and C. Borges. Data Supplement to Impedance Examples (Version 1.1), June 2024. URL https://doi.org/10.5281/zenodo.12559924.

[7] T. Askham, C. Borges, J. Hoskins, and M. Rachh. Random walks in frequency and the reconstruction of obstacles with cavities from multi-frequency data. *Journal of Scientific Computing*, 98(1):15, 2023. URL https://doi.org/10.1007/s10915-023-02406-z.

[8] T. Askham, C. Borges, J. Hoskins, and M. Rachh. askhamwhat/impedance-examples: version 1.1, June 2024. URL https://doi.org/10.5281/zenodo.12559791.

[9] T. Askham, M. Rachh, M. O'Neil, J. Hoskins, D. Fortunato, S. Jiang, F. Fryklund, T. Goodwill, H. Y. Wang, and H. Zhu. chunkIE: a MATLAB integral equation toolbox, June 2024. URL https://github.com/fastalgorithms/chunkie.

[10] B. Aslanyürek and H. Sahintürk. Reconstruction of thickness variation of a dielectric coating through the generalized impedance boundary conditions. *ESAIM: Mathematical Modelling and Numerical Analysis*, 48(4): 1011–1027, 2014. URL https://doi.org/10.1051/m2an/2013131.

[11] H. Attouch, J. Bolte, P. Redont, and A. Soubeyran. Proximal alternating minimization and projection methods for nonconvex problems: An approach based on the kurdyka-łojasiewicz inequality. *Mathematics of Operations Research*, 35(2):438–457, 2010. ISSN 0364765X, 15265471. URL http://www.jstor.org/stable/40801236.

[12] G. Bao and P. Li. Inverse medium scattering for three-dimensional time harmonic maxwell equations. *Inverse Problems*, 20(2):L1, 2004. URL https://doi.org/10.1088/0266-5611/20/2/L01.

[13] G. Bao and P. Li. Inverse medium scattering problems for electromagnetic waves. *SIAM Journal on Applied Mathematics*, 65(6):2049–2066, 2005. URL https://doi.org/10.1137/040607435.

[14] G. Bao and P. Li. *Shape reconstruction of inverse medium scattering for the Helmholtz equation*, volume 56. Higher Education Press Beijing, 2012. URL https://doi.org/10.1515/9783110259056.283.

[15] G. Bao, S. Hou, and P. Li. Inverse scattering by a continuation method with initial guesses from a direct imaging algorithm. *Journal of Computational Physics*, 227(1):755–762, 2007. URL https://doi.org/10.1016/j.jcp.2007.08.020.

[16] G. Bao, P. Li, J. Lin, and F. Triki. Inverse scattering problems with multi-frequencies. *Inverse Problems*, 31(9):093001, 2015. URL https://doi.org/10.1088/0266-5611/31/9/093001.

[17] D. Beylkin and V. Rokhlin. Fitting a bandlimited curve to points in a plane. *SIAM Journal on Scientific Computing*, 36(3):A1048–A1070, 2014. URL https://doi.org/10.1137/130932703.

[18] J. Blauert and N. Xiang. *Dissipation, Reflection, Refraction, and Absorption*, pages 145–160. Springer Berlin Heidelberg, Berlin, Heidelberg, 2009. ISBN 978-3-642-03393-3. doi: 10.1007/978-3-642-03393-3_11. URL https://doi.org/10.1007/978-3-642-03393-3_11.

[19] J. Bolte, S. Sabach, and M. Teboulle. Proximal alternating linearized minimization for nonconvex and nonsmooth problems. *Mathematical Programming*, 146(1-2):459–494, 2014. URL https://doi.org/10.1007/s10107-013-0701-9.

[20] C. Borges and L. Greengard. Inverse Obstacle Scattering in Two Dimensions with Multiple Frequency Data and Multiple Angles of Incidence. *SIAM J. Imaging Sciences*, 8(1):280–298, 2015. doi: 10.1137/140982787. URL http://dx.doi.org/10.1137/140982787.

[21] C. Borges and M. Rachh. Multifrequency inverse obstacle scattering with unknown impedance boundary conditions using recursive linearization. *Advances in Computational Mathematics*, 48(1):2, 2022. URL https://doi.org/10.1007/s10444-021-09915-1.

[22] C. Borges, A. Gillman, and L. Greengard. High resolution inverse scattering in two dimensions using recursive linearization. *SIAM Journal on Imaging Sciences*, 10(2):641–664, 2017. URL https://doi.org/10.1137/16M1093562.

[23] L. Bourgeois and H. Haddar. Identification of generalized impedance boundary conditions in inverse scattering problems. *Inverse Problems and Imaging*, 4(1):19–38, 2010. ISSN 1930-8337. URL https://doi.org/10.3934/ipi.2010.4.19.

[24] L. Bourgeois, N. Chaulet, and H. Haddar. Stable reconstruction of generalized impedance boundary conditions. *Inverse Problems*, 27(9):095002, 2011. URL https://doi.org/10.1088/0266-5611/27/9/095002.

[25] L. Bourgeois, N. Chaulet, and H. Haddar. On simultaneous identification of the shape and generalized impedance boundary condition in obstacle scattering. *SIAM Journal on Scientific Computing*, 34(3):A1824–A1848, 2012. URL https://doi.org/10.1137/110850347.

[26] J. Bremer, Z. Gimbutas, and V. Rokhlin. A nonlinear optimization procedure for generalized gaussian quadratures. *SIAM Journal on Scientific Computing*, 32(4):1761–1788, 2010.

[27] O. Bruno, T. Elling, and C. Turc. Regularized integral equations and fast high-order solvers for sound-hard acoustic scattering problems. *International Journal for Numerical Methods in Engineering*, 91(10):1045–1072, 2012. URL https://doi.org/10.1002/nme.4302.

[28] F. Cakoni and R. Kress. Integral equation methods for the inverse obstacle problem with generalized impedance boundary condition. *Inverse Problems*, 29(1):015005, 2012. URL https://doi.org/10.1088/0266-5611/29/1/015005.

[29] A. Carpio, S. Iakunin, and G. Stadler. Bayesian approach to inverse scattering with topological priors. *Inverse Problems*, 36(10):105001, 2020. URL https://doi.org/10.1088/1361-6420/abaa30.

[30] G. Chavent, G. Papanicolaou, P. Sacks, and W. Symes. *Inverse Problems in Wave Propagation*. The IMA Volumes in Mathematics and its Applications. Springer New York, 2012. ISBN 9781461218784. URL https://books.google.com/books?id=IhfSBwAAQBAJ.

[31] Y. Chen. Recursive linearization for inverse scattering. *Mathematical and numerical aspects of wave propagation (Golden, CO, 1998)*, pages 114–117, 1995.

[32] Y. Chen. Inverse scattering via Heisenberg's uncertainty principle. *Inverse Problems*, 13(2):253, 1997. URL http://doi.org/10.1088/0266-5611/13/2/005.

[33] M. Cheney and B. Borden. *Fundamentals of Radar Imaging*. CBMS-NSF Regional Conference Series in Applied Mathematics. Society for Industrial and Applied Mathematics, 2009. URL https://books.google.com/books?id=E7M7HQGB0EwC.

[34] M. D. Collins and W. A. Kuperman. Inverse problems in ocean acoustics. *Inverse Problems*, 10(5):1023, 1994. URL http://stacks.iop.org/0266-5611/10/i=5/a=003.

[35] R. Collins. *Nondestructive Testing of Materials*. Studies in applied electromagnetics and mechanics. IOS Press, 1995. ISBN 9789051992397. URL https://books.google.com/books?id=E55RFcv-rGMC.

[36] D. L. Colton and R. Kress. *Inverse acoustic and electromagnetic scattering theory*, volume 93. Springer, 1998. URL https://doi.org/10.1007/978-3-662-03537-5.

[37] A. R. Conn, N. I. M. Gould, and P. L. Toint. *Trust region methods*. SIAM, 2000. URL https://doi.org/10.1137/1.9780898719857.

[38] H. Engl, A. K. Louis, and W. Rundell. *Inverse Problems in Medical Imaging and Nondestructive Testing: Proceedings of the Conference in Oberwolfach, Federal Republic of Germany, February 4–10, 1996*. Springer Vienna, 2012. ISBN 9783709165218. URL https://books.google.com/books?id=ttHuCAAAQBAJ.

[39] E. M. Gafni and D. P. Bertsekas. Convergence of a gradient projection method. Technical Report LIDS-P-1201, Laboratory for Information and Decision Systems, Massachusetts Institute of Technology, May 1982. URL http://hdl.handle.net/1721.1/2803.

[40] J. Guo, G. Yan, and M. Cai. Multilayered scattering problem with generalized impedance boundary condition on the core. *Journal of Applied Mathematics*, 2015, 2015. URL https://doi.org/10.1155/2015/195460.

[41] H. Haddar, P. Joly, and H. M. Nguyen. *Asymptotic Models for Scattering from Strongly Absorbing Obstacles: the Scalar Case*. PhD thesis, INRIA, 2004. URL https://inria.hal.science/inria-00070793.

[42] J. Helsing. Solving integral equations on piecewise smooth boundaries using the rcip method: a tutorial. In *Abstract and applied analysis*, number 1 in 2013, page 938167. Wiley Online Library, 2013.

[43] O. Ivanyshyn and R. Kress. Inverse scattering for surface impedance from phase-less far field data. *Journal of Computational Physics*, 230(9):3443–3452, 2011. URL https://doi.org/10.1016/j.jcp.2011.01.038.

[44] O. Ivanyshyn Yaman. Reconstruction of generalized impedance functions for 3d acoustic scattering. *Journal of Computational Physics*, 392:444–455, 2019. URL https://doi.org/10.1016/j.jcp.2019.04.060.

[45] Y. Q. Jin. *Theory and Approach of Information Retrievals from Electromagnetic Scattering and Remote Sensing*. Springer Netherlands, 2006. ISBN 9781402040306. URL https://books.google.com/books?id=XOWQZ61M0X0C.

[46] D. S. Jones. An improved surface radiation condition. *IMA journal of applied mathematics*, 48(2):163–193, 1992. URL https://doi.org/10.1093/imamat/48.2.163.

[47] R. Kress. Integral equation methods in inverse obstacle scattering with a generalized impedance boundary condition. In *Contemporary Computational Mathematics-A Celebration of the 80th Birthday of Ian Sloan*, pages 721–740. Springer, 2018. URL https://doi.org/10.1007/978-3-319-72456-0_32.

[48] R. Kress. Some old and some new results in inverse obstacle scattering. *Maxwell's Equations: Analysis and Numerics*, 24:259, 2019. URL https://doi.org/10.1515/9783110543612-008.

[49] R. Kress and W. Rundell. Inverse scattering for shape and impedance. *Inverse problems*, 17(4):1075, 2001. URL https://doi.org/10.1088/0266-5611/17/4/334.

[50] R. Kress and W. Rundell. Inverse scattering for shape and impedance revisited. *Journal of Integral Equations and Applications*, 30(2):293–311, 2018. URL https://doi.org/10.1216/JIE-2018-30-2-293.

[51] K. Kreutz-Delgado. The complex gradient operator and the cr-calculus. *arXiv preprint arXiv:0906.4835*, 2009.

[52] P. Kuchment. *The Radon Transform and Medical Imaging*. CBMS-NSF Regional Conference Series in Applied Mathematics. Society for Industrial and Applied Mathematics, 2014. ISBN 9781611973280. URL http://doi.org/10.1137/1.9781611973297.

[53] K. J. Langenberg, K. Mayer, P. Fellinger, and R. Marklein. Imaging and Inverse Scattering in Nondestructive Evaluation with Acoustic and Elastic Waves. In *Acoustical Imaging*, pages 165–172. Springer, 1993. URL https://doi.org/10.1007/978-1-4615-2958-3_22.

[54] K. M. Lee. An inverse scattering problem from an impedance obstacle. *Journal of Computational Physics*, 227(1):431–439, 2007. URL https://doi.org/10.1016/j.jcp.2007.07.030.

[55] M. Z. Nashed and O. Scherzer. *Inverse Problems, Image Analysis, and Medical Imaging: AMS Special Session on Interaction of Inverse Problems and Image Analysis, January 10-13, 2001, New Orleans, Louisiana*. Contemporary mathematics - American Mathematical Society. American Mathematical Society, 2002. ISBN 9780821856499. URL https://books.google.com/books?id=63TlxnJt4k0C.

[56] J. V. Neumann. On rings of operators. reduction theory. *Annals of Mathematics*, 50(2):401–485, 1949. ISSN 0003486X. URL http://www.jstor.org/stable/1969463.

[57] H. H. Qin and D. Colton. The inverse scattering problem for cavities with impedance boundary condition. *Advances in Computational Mathematics*, 36(2):157–174, 2012. URL https://doi.org/10.1007/s10444-011-9179-2.

[58] S. M. Rytov. Calcul du skin-effect par la méthode des perturbations. *J. Phys. USSR*, 2(3):233–242, 1940.

[59] O. Scherzer. *Handbook of Mathematical Methods in Imaging*. Handbook of Mathematical Methods in Imaging. Springer New York, 2010. ISBN 9780387929194. URL https://books.google.com/books?id=FzvNfkMjvPwC.

[60] T. B. A. Senior. Impedance boundary conditions for imperfectly conducting surfaces. *Applied Scientific Research, Section B*, 8(1):418–436, 1960. URL https://doi.org/10.1007/BF02920074.

[61] T. B. A. Senior. Approximate boundary conditions for homogeneous dielectric bodies. *Journal of electromagnetic waves and applications*, 9(10): 1227–1239, 1995. URL https://doi.org/10.1163/156939395X00019.

[62] T. B. A. Senior. Generalized boundary conditions for scalar fields. *The Journal of the Acoustical Society of America*, 97(6):3473–3477, 1995. URL https://doi.org/10.1121/1.412433.

[63] T. B. A. Senior and J. L. Volakis. *Approximate boundary conditions in electromagnetics*. Number 41 in IEEE Electromagnetic Waves Series. The Institution of Electrical Engineers, 1995. URL https://doi.org/10.1049/PBEW041E.

[64] T. B. A. Senior, J. L. Volakis, and S. R. Legault. Higher order impedance and absorbing boundary conditions. *IEEE Transactions on Antennas and Propagation*, 45(1):107–114, 1997. URL https://doi.org/10.1109/8.554247.

[65] P. Serranho. A hybrid method for inverse scattering for shape and impedance. *Inverse Problems*, 22(2):663, 2006. URL https://doi.org/10.1088/0266-5611/22/2/017.

[66] F. Simonetti. Inverse scattering in modern ultrasound imaging. *The Journal of the Acoustical Society of America*, 123(5):3915–3915, 2008. URL https://doi.org/10.1121/1.2935927.

[67] M. Sini and N. T. Thanh. Inverse acoustic obstacle scattering problems using multifrequency measurements. *Inverse Problems and Imaging*, 6(4): 749–773, 2012. URL https://doi.org/10.3934/ipi.2012.6.749.

[68] R. T. Smith. An inverse acoustic scattering problem for an obstacle with an impedance boundary condition. *Journal of mathematical analysis and applications*, 105(2):333–356, 1985. URL https://doi.org/10.1016/0022-247X(85)90052-6.

[69] C. Turc, Y. Boubendir, and M. K. Riahi. Well-conditioned boundary integral equation formulations and nyström discretizations for the solution of helmholtz problems with impedance boundary conditions in two-dimensional lipschitz domains. *The Journal of Integral Equations and Applications*, 29(3):441–472, 2017. URL https://www.jstor.org/stable/26407485.

[70] E. Ustinov. *Encyclopedia of Remote Sensing*, chapter Geophysical Retrieval, Inverse Problems in Remote Sensing, pages 247–251. Springer New York, New York, NY, 2014. ISBN 978-0-387-36699-9. doi: 10.1007/978-0-387-36699-9_54. URL http://dx.doi.org/10.1007/978-0-387-36699-9_54.

[71] D. S. Wang. Limits and validity of the impedance boundary condition on penetrable surfaces. *IEEE transactions on antennas and propagation*, 35 (4):453–457, 1987. URL https://doi.org/10.1109/TAP.1987.1144125.

[72] S. J. Wright. Coordinate descent algorithms. *Mathematical programming*, 151(1):3–34, 2015. URL https://doi.org/10.1007/s10107-015-0892-3.

[73] J. Yang, B. Zhang, and H. Zhang. Reconstruction of complex obstacles with generalized impedance boundary conditions from far-field data. *SIAM Journal on Applied Mathematics*, 74(1):106–124, 2014. URL https://doi.org/10.1137/130921350.

[74] E. H. Zarantonello. Projections on convex sets in hilbert space and spectral theory: Part i. projections on convex sets: Part ii. spectral theory. In *Contributions to nonlinear functional analysis*, pages 237–424. Elsevier, 1971. URL https://doi.org/10.1016/B978-0-12-775850-3.50013-3.

A Integral equation formulations of the PDEs and their numerical discretization

To solve the forward impedance and transmission problems, we reformulate the partial differential equations, i.e. (1) and (2), using well-established methods from layer potential theory [36]. We briefly describe the representations and numerical methods we use in this section.

Consider an obstacle, Ω_1, with a smooth boundary curve, Γ. Let $G^k(\mathbf{x},\mathbf{y}) = \imath H_0^{(1)}(k\|\mathbf{x}-\mathbf{y}\|)/4$ be the Green's function for the two dimensional Helmholtz equation and $\mathbf{n}$ be the outward normal to the obstacle boundary, Γ. Let S_k and D_k denote the single and double layer operators, respectively, i.e.

$$S_k\sigma(\mathbf{x}) = \int_\Gamma G^k(\mathbf{x},\mathbf{y})\sigma(\mathbf{y})ds(\mathbf{y}), \quad D_k\sigma(\mathbf{x}) = \int_\Gamma \frac{\partial G^k(\mathbf{x},\mathbf{y})}{\partial \mathbf{n}(\mathbf{y})}\sigma(\mathbf{y})ds(\mathbf{y}) \ ,$$

for $\mathbf{x} \in \mathbb{R}^2 \setminus \Gamma$. For $\mathbf{x} \in \Gamma$, we denote these operators by $\mathcal{S}_k$ and $\mathcal{D}_k$, respectively. We denote the normal derivatives of S_k and D_k by $\mathcal{K}_k$ and $\mathcal{T}_k$, respectively, i.e.

$$\mathcal{K}_k\phi(\mathbf{x}) = \int_\Gamma \frac{\partial G^k(\mathbf{x},\mathbf{y})}{\partial \mathbf{n}(\mathbf{x})}\phi(\mathbf{y})ds(\mathbf{y}),$$

and

$$\mathcal{T}_k\phi(\mathbf{x}) = \text{f. p.} \int_\Gamma \frac{\partial^2 G^k(\mathbf{x},\mathbf{y})}{\partial \mathbf{n}(\mathbf{x})\mathbf{n}(\mathbf{y})}\phi(\mathbf{y})ds(\mathbf{y}) \ ,$$

where $\mathbf{x} \in \Gamma$ and f. p. indicates that the integral is interpreted in the Hadamard finite part sense.

On smooth curves, $\mathcal{S}_k$, $\mathcal{D}_k$, and $\mathcal{K}_k$ are weakly singular integral operators, while $\mathcal{T}_k$ is hyper-singular.

A.1 Transmission problem

To solve the transmission problem, we represent the scattered field inside the obstacle, denoted $u^{\rm scat}_{k_1}$, and outside the obstacle, denoted $u^{\rm scat}_{k_2}$, as

$$\begin{aligned} u^{\rm scat}_{k_1} &= -u^{\rm inc} + \frac{1}{b_1} D_{k_1}\mu - \frac{1}{b_1} S_{k_1}\sigma \\ u^{\rm scat}_{k_2} &= \frac{1}{b_2} D_{k_2}\mu - \frac{1}{b_2} S_{k_2}\sigma \end{aligned} \tag{29}$$

where μ and σ are unknown densities defined on Γ and $b_1 = \alpha = 1/(\rho_r(1+\imath\delta/\omega))$ and $b_2 = 1$.

Applying the boundary conditions in (1) to the representation (29) we obtain the system of boundary integral equations

$$\begin{bmatrix} I + \frac{1}{qb_2}\mathcal{D}_{k_2} - \frac{1}{qb_1}\mathcal{D}_{k_1} & -\left(\frac{1}{qb_2}\mathcal{S}_{k_2} - \frac{1}{qb_1}\mathcal{S}_{k_1}\right) \\ \mathcal{T}_{k_2} - \mathcal{T}_{k_1} & I - (\mathcal{K}_{k_2} - \mathcal{K}_{k_1}) \end{bmatrix} \begin{bmatrix} \mu \\ \sigma \end{bmatrix} = \begin{bmatrix} -\frac{1}{q} u^{\rm inc} \\ -b_2 \frac{\partial u^{\rm inc}}{\partial n} \end{bmatrix} , \tag{30}$$

where $q = (1/b_1 + 1/b_2)/2$. This system is Fredholm and has a unique solution for the wavenumbers treated in this paper. While $\mathcal{T}_{k_i}$ is hyper-singular for $i = 1, 2$, the operator $\mathcal{T}_{k_2} - \mathcal{T}_{k_1}$ is weakly singular owing to cancellations in the singularities.

A.2 Impedance problem

To solve the impedance and Neumann ($\lambda = 0$) problems, we use the regularized combined layer potential representation proposed and analyzed in [27, 69]. In particular, we adopt the representation

$$u^{\rm scat} = \left(S_{k_2} + \imath k_2 D_{k_2} \mathcal{S}_{\imath|k_2|}\right)\phi \, . \tag{31}$$

Applying the boundary conditions in (2) to the representation (31) and applying Calderon identities, gives the boundary integral equation

$$\begin{aligned} \Bigg[-\frac{2+\imath k_2}{4} I + \mathcal{K}_{k_2} + \imath k_2 \left(\left(\mathcal{T}_{k_2} - \mathcal{T}_{\imath|k_2|}\right) \mathcal{S}_{\imath|k_2|} + \left(\mathcal{K}_{\imath|k_2|}\right)^2 \right) + \imath k_2 \lambda \Bigg(S_{k_2} + \\ \imath k_2 \mathcal{D}_{k_2} \mathcal{S}_{\imath|k_2|} + \frac{\imath k_2}{2} \mathcal{S}_{\imath|k_2|} \Bigg) \Bigg] \phi = -\left(\frac{\partial u^{\rm inc}}{\partial n} + \imath k_2 \lambda u^{\rm inc} \right) , \end{aligned} \tag{32}$$

which is Fredholm and has a unique solution when $2 + \imath k_2 \neq 0$. Similar to the above, $\mathcal{T}_{k_2} - \mathcal{T}_{\imath|k_2|}$ is a weakly singular operator, so that the calculations can be arranged with all integral kernels used being weakly singular.

A.3 Numerical Solution

The Nyström method can be used to solve both systems (30) and (32). We discretize the boundary Γ using $N = \mathcal{O}(k)$, with approximately 10 points per

wavelength, where for the impedance boundary condition $k = k_2$ and for the transmission problem $k = \max(k_1, k_2)$. To discretize the weakly singular integral operators we apply the Hybrid Gauss-trapezoidal quadrature rule of order 16 from [2].

For the special case of the "L"-shaped domain in Section 4.3, we apply a different solver. To solve the resulting boundary integral equation, whose solution develops singularities at the corners, we apply the recursively compressed inverse pre-conditioner (RCIP) scheme of [42] which is available in the `chunkie` MATLAB package [9]. This software is based on dividing the boundary into panels, each of which is approximated by a 16th order Legendre interpolant. The panels are divided so that they are no longer than $4/k_2$ (similar to a points-per-wavelength requirement). The weakly-singular integrals in the BIE are computed using generalized Gaussian quadrature [26]. The RCIP scheme effectively solves the problem using a dyadically refined mesh near the corners; we select 40 levels of refinement. The accuracy of the solver is then tested against an analytic solution. In the examples in the paper, there are at least ten digits of precision in these tests (often more).

We invert the resulting linear system directly using Gaussian elimination at the cost of $\mathcal{O}(k^3)$ operations. We store the inverse, so this work is amortized over incident directions and the inverse can be applied in $\mathcal{O}(k^2)$ operations per incident field to generate forward data. With $\mathcal{O}(k)$ incident fields, the total work at a given frequency is then $\mathcal{O}(k^3)$ for generating data and for evaluating the objective function. In the inverse problem, filling the Jacobian matrix, as described in Section 3.2, requires $\mathcal{O}(k)$ PDE solves per incident direction resulting in $\mathcal{O}(k^4)$ total work at a given frequency. These costs can be reduced by using alternate optimization methods or by employing fast methods for the PDE solutions but this was not a focus of the present work.